Chemical Engineering Journal 541 (2026) 177727

Contents lists available at ScienceDirect

Chemical Engineering Journal

journal homepage: www.elsevier.com/locate/cej

A novel $CaTiO_3/WO_3/BiVO_4$ heterostructured photoanode for simultaneous glycerol valorization and hydrogen evolution

Leonardo A. Delgado [a], Ivan Merino-Garcia [b], Sara Crespo [b], Kevin Fernández-Caso [b,c], Vítor J.P. Vilar [a], Francisca C. Moreira [a,*], Jonathan Albo [b,*]

[a] LSRE-LCM, ALiCE, Faculty of Engineering, University of Porto, Rua Dr. Roberto Frias, 4200-465, Porto, Portugal
[b] Departamento de Ingenierías Química y Biomolecular, Universidad de Cantabria, Avenida de los Castros s/n, Santander, 39005, Spain
[c] Process & Energy Department, Faculty of Mechanical Engineering, Delft University of Technology, Leeghwaterstraat 39, Delft, 2628, CB, the Netherlands

ARTICLE INFO

Keywords:
Waste-to-chemicals
Photoelectrocatalysis
Photoelectrodes
Heterostructured photoanode
Flow electrochemistry
Electrolyzers

ABSTRACT

The development of photoelectrochemical (PEC) systems for glycerol valorization and green hydrogen (H_2) production is crucial for advancing sustainable energy technologies. In this work, a novel multilayer $CaTiO_3/WO_3/BiVO_4$ (CWB) heterostructured photoanode was fabricated *via* automated spray-coating to promote efficient charge separation and enable glycerol photoelectrooxidation, with photogenerated electrons delivered to a dark cathode to drive the hydrogen evolution reaction (HER). The CWB photoanode operated in a filter-press flow cell, facilitating selective glycerol photoelectrooxidation toward valuable C_1–C_3 compounds, while H_2 was simultaneously produced at a platinum plate dark cathode. At a current density of −10 mA cm^{-2} under visible light illumination, glycerol conversion yielded dihydroxyacetone (DHA), glyceric acid (GEA), and formate ($HCOO^-$) with an overall Faradaic efficiency (FE) of 64%, achieving a DHA production rate of 124 μmol m^{-2} s^{-1}. Concurrently, H_2 was produced at the cathode with a production rate of 549 μmol m^{-2} s^{-1}, corresponding to an energy consumption (E_{Con}) of 383 kWh $kmol^{-1}$ and a cathodic energy efficiency (CEE) of 74%. The improved performance is attributed to enhanced charge separation promoted by the multilayer heterostructure, with efficient electron transfer across the $WO_3/BiVO_4$ interface and improved charge collection through the $CaTiO_3$ layer. These findings demonstrate that replacing the oxygen evolution reaction (OER) with glycerol photoelectrooxidation in multilayer heterostructured photoanodes enables simultaneous H_2 production and generation of value-added chemicals, providing a promising platform for integrated PEC systems.

1. Introduction

The rapid expansion of biodiesel production has led to a significant accumulation of crude glycerol, a byproduct of the transesterification process, representing approximately 10 wt% of each biodiesel batch [1,2]. The oversupply of glycerol, combined with its low market value and high purification costs, has transformed this compound into an underutilized waste stream, posing both economic and environmental challenges [3,4].

To address this issue, several glycerol valorization strategies have been explored, including biological [5–7], thermochemical [8–10], catalytic [11,12], and electrochemical [13,14] processes. Among them, electrochemical (EC) and photoelectrochemical (PEC) techniques have demonstrated potential in the conversion of glycerol *via* hydroxyl (–OH) and C—C cleavage oxidations into a variety of C_1 to C_3 compounds on the anode, such as formic acid (FA), glyceric acid (GEA), and dihydroxyacetone (DHA) However, controlling selectivity remains a major challenge due to the coexistence of multiple competing reaction pathways, where small changes in reaction conditions can shift the reaction from partial oxidation toward C—C bond cleavage or complete mineralization [15]. Conventional electrochemical systems for hydrogen evolution reaction (HER) or CO_2 reduction (CO_2RR) typically suffer from high overall energy consumption, largely because the anodic oxygen evolution reaction (OER) is kinetically sluggish and requires large overpotentials [16]. Despite their potential advantages, PEC strategies for glycerol oxidation remain underexplored and are predominantly focused on complete mineralization rather than selective conversion to value-added product. Replacing the OER (Eq. (1) [17]) with the glycerol PEC oxidation reaction (GPEOR, Eq. (2) [18]), both in alkaline medium, represents a promising strategy. This approach might reduce energy

* Corresponding authors.
E-mail addresses: franciscam@fe.up.pt (F.C. Moreira), jonathan.albo@unican.es (J. Albo).

https://doi.org/10.1016/j.cej.2026.177727
Received 29 January 2026; Received in revised form 20 May 2026; Accepted 25 May 2026
Available online 25 May 2026

consumption by over 50% while simultaneously generating valuable products at the anode.

Moreover, GPEOR can be coupled with cathodic reactions, such as the HER or CO_2RR, both in alkaline medium, to enhance the overall efficiency of the system [19–25].

$$(\text{OER})\ 4\ OH^- \rightarrow O_2 + 2\ H_2O + 4\ e^-\ E^0 = +1.23\ \text{V}\ vs.\text{RHE} \quad (1)$$

$$(\text{GPEOR})\ C_3H_8O_3 + n\ OH^- \xrightarrow{h\nu \geq E_{bg}} \text{Products} + x\ H_2O + n\ e^- \quad (2)$$

$$(\text{HER})\ 2\ H_2O + 2\ e^- \rightarrow H_2 + 2\ OH^-\ E^0 = 0\ \text{V}\ vs.\text{RHE} \quad (3)$$

$$(CO_2\text{RR})\ CO_2 + H_2O + 2e^- \rightarrow HCOO^- + OH^-\ E^0 = -0.64\ \text{V}\ vs.\text{RHE} \quad (4)$$

The performance of GPEOR is strongly governed by the properties of semiconductor photoanodes, particularly their ability to harvest light, promote charge separation, and ensure efficient charge transport [26,27]. Metal oxides such as bismuth vanadate ($BiVO_4$), calcium titanate ($CaTiO_3$), and tungsten trioxide (WO_3) have been widely explored due to their stability, abundance, and suitable band structures [28–32]. These materials are characterized by strong ionic bonding and offer several benefits, such as: earth-abundant, low-cost, eco-friendly nature, unique optical properties, high chemical and thermal stability, small optical band gap, and high dielectric constants [33]. In particular, n-type metal oxide semiconductors are often used due to their appropriate band edge potential and their ability to donate electrons, resulting from an excess of electrons [34,35]. To overcome the intrinsic limitations of single-component photoanodes, multilayer architectures combining complementary metal oxides have been extensively explored. The incorporation of heterojunctions such as $CaTiO_3/BiVO_4$ and $BiVO_4/WO_3$ has been reported to improve light absorption, promote efficient charge separation, and suppress bulk and interfacial recombination losses. $CaTiO_3$, a perovskite-type catalyst with the general formula ABO_3, typically has an orthorhombic (pseudocubic) crystal structure, formed by 3D networks of corner-sharing BO_6 octahedra, with alkaline earth metal occupying the A-site. This unique structure facilitates enhanced charge carrier separation and high electron mobility [36]. Furthermore, Type II heterojunctions offer a promising solution to overcome the limitations of $BiVO_4$ by improving optical absorption, expanding the interfacial area, and facilitating efficient charge separation [37]. Studies demonstrated that $BiVO_4$ has a narrow bandgap ($E_g \approx 2.4$ eV), ensuring efficient light harvesting, but suffers from faster e^-_{CB}/h^+_{VB} recombination due to its lower electron mobility [38]. Meanwhile, WO_3 governs charge transport in the system, reducing bulk recombination and enhancing overall charge collection efficiency, due to a lower CB (+0.4 V *vs.* RHE at pH 0) and a bandgap of 2.5–2.8 eV, enhancing charge transfer [39].

Herein, we report the development of a novel multilayered n-n-type heterojunction material composed of $CaTiO_3/WO_3/BiVO_4$ (CWB) with a 21:16:63 mass ratio, fabricated *via* an automated and reproducible spray-coating technique. This CWB photoanode, designed for back-illumination, was employed for the selective GPEOR to produce value-added C_1–C_3 compounds. The system was operated in a single-pass filter-press flow cell using an aqueous glycerol solution as the anolyte, enabling the simultaneous glycerol oxidation at the photoanode and H_2 evolution at a platinized titanium cathode in the dark. The PEC response was evaluated by monitoring the cathodic current upon photoanode illumination. The CWB material was thoroughly characterized both physicochemically and photoelectrochemically.

2. Material and methods

2.1. Chemicals

The reagents used in this work included $CaTiO_3$, WO_3, and $BiVO_4$ for photoanode fabrication. Isopropanol and Nafion for ink preparation. Potassium carbonate ($KHCO_3$) and glycerol for electrolyte preparations. Potassium hydroxide (KOH) for membrane activation, and sulfuric acid (H_2SO_4), acetonitrile (CH_3CN), and sodium carbonate (Na_2CO_3) for product analysis. All solutions were prepared with ultrapure water. Detailed information regarding reagents and specifications is provided in the Supporting Information.

2.2. Fabrication of CWB photoanodes

Fluorine-coated tin oxide (FTO, 2.2 mm, 12–15 Ω sq.$^{-1}$, MSE supplies) glass substrates with a geometric area of 35 mm × 35 mm were cleaned by ultrasonication and used as supports for catalyst deposition. Catalyst ink loadings were 1 mg cm^{-2} ($CaTiO_3$), 0.75 mg cm^{-2} (WO_3), and 3 mg cm^{-2} ($BiVO_4$) (Fig. S1) [40,41]. The inks were prepared using isopropanol and Nafion (70:30 wt%), as detailed in Table S1. The ink was deposited onto FTO by automated spray-coating. Deposition was carried out at 65 °C with a controlled flow rate (10–20 mL h^{-1}) and nozzle distance (33 mm). Additional details regarding substrate preparation, ink formulation, and deposition parameters are provided in the Supporting Information.

2.3. Morphological and optical characterization of CWB photoanodes

Morphology and elemental composition were analyzed by scanning electron microscopy and energy dispersive X-ray spectroscopy (SEM-EDS, FEI Quanta 400 FEG ESEM) coupled with an EDAX Genesis X4M system. Samples (fresh and used) were mounted on carbon tape, sputter-coated with gold/palladium (Au/Pd) layer, and analyzed at 15 kV using secondary electron and *Z*-contrast modes, with EDS spectra and elemental maps collected from representative regions. Surface chemical composition was determined by X-ray photoelectron spectroscopy (XPS, Kratos Axis Ultra HAS) using a monochromated Al Kα X-ray source (1486.6 eV) with samples pressed and mounted on conductive carbon tape; survey and high-resolution spectra were acquired at pass energies of 160 and 40 eV, respectively. Specific surface area was determined by N_2 physisorption at 77 K using a Micromeritics 3Flex analyzer after degassing at 150 °C for 4 h, with Brunauer-Emmett-Teller (BET) surface area calculated from adsorption isotherms in the relative pressure range of 0.05–0.30. Crystalline structure and phase composition were analyzed by X-ray diffraction (XRD, Bruker D8 Advance, Cu Kα, λ = 1.5406 Å) over the 2θ range of 5–100° with a step size of 0.02°. Crystallite size (D), microstrain (ε), dislocation density (δ), and interplanar spacing (d_{hkl}) were calculated using Eqs. (5), (6), (7), and (8) [42].

$$D\ [\text{nm}] = \frac{K\lambda}{\beta\cos\theta} \quad (5)$$

$$\varepsilon\ [\text{a.u.}] = \frac{\beta}{4\tan\theta} \quad (6)$$

$$\delta\ [\text{lines m} - 2] = \frac{1}{D^2} \quad (7)$$

$$d_{hkl}\ [\text{nm}] = \frac{\lambda}{2\sin\theta} \quad (8)$$

where K is the factor (typically 0.94), λ is the x-ray wavelength (in Å), β is the full width at half maximum of the selected peak (FWHM, in radians), and θ is the Bragg angle (in radians). Additional experimental details are provided in the Supporting Information.

2.4. Experimental setup for PEC trials

Fig. S2 illustrates the filter-press flow reactor (Micro Flow Cell from ElectroCell, Denmark) used for PEC trials. This system comprised distinct cathodic and anodic compartments, separated by a Nafion® 117 proton exchange membrane (PEM; thickness: 0.180 mm; exchange capacity: >0.9 meq g^{-1}; Ion Power). Prior to use, the membrane was

activated in 1.0 M KOH for 24 h and rinsed with ultrapure water. This preparation enhanced proton (H^+) transport through the polymer structure, reducing mass-transfer limitations while effectively preventing chemical crossover and re-oxidation [43,44]. The photoanode (10 cm^2) was illuminated under a back-side configuration using an LED lamp (Photolab LED 450–3, Apria Systems) at an intensity of 100 mW cm^{-2} (equivalent to 1 sun). A platinized-titanium plate was used as the cathode and a leakless silver-silver chlorideAg/AgCl (3.4 M KCl) electrode as the reference. The electrodes were assembled in a flow-through configuration using PVDF flow frames with integrated turbulence promoters and sealed with EPDM gaskets. A carbon sheet served as current collector, and a transparent methacrylate plate allowed light transmission to the photoanode. The cell components were compressed between PTFE end plates and stainless-steel supports to ensure sealing and stable operation.

For cathodic response influenced by CWB photoanode illumination, both compartments were fed with a 0.5 M aqueous solution (pH 8.7). Linear sweep voltammetry (LSV), chronopotentiometry (CP), and electrochemical impedance spectroscopy (EIS) were carried out under illumination (100 mW cm^{-2}) and dark conditions using a potentiostat–galvanostat, as detailed in the Supporting Information. The measurements included: (i) LSV between −1.7 V and − 0.8 V (*vs.* Ag/AgCl) at a scan rate of 50 mV s^{-1} under light (100 mW cm^{-2}) and dark conditions; (ii) CP at different current densities (*j*) of −10, −45, −90, and − 200 mA cm^{-2} during 60 min under light (100 mW cm^{-2}) conditions; and (iii) EIS at 0.8 V (*vs.* Ag/AgCl) over a frequency range of 10^{-1} to 10^5 Hz under light (100 mW cm^{-2}) and dark conditions.

For GPEOR experiments (Fig. 1), the anolyte consisted of 1.0 M glycerol in 0.5 M $KHCO_3$, while 0.5 M $KHCO_3$ was used as the catholyte under continuous single-pass operation. The anolyte was periodically sampled and acidified to prevent product degradation. Liquid products (DHA and GEA) were quantified by HPLC, while $HCOO^-$ was analyzed by ion chromatography. H_2 production was monitored online using gas chromatography. Detailed experimental conditions and analytical parameters can be found in Fig. S3.

2.4.1. Calculations

The efficiency of the GPEOR to value-added products coupled to H_2 production was evaluated using efficiency parameters: production rate (*r*), Faradaic efficiency (FE), product selectivity (S_i), energy consumption (E_{Con}), and cathodic energy efficiency (CEE).

The *r* refers to the rate at which a specific product is formed. It was determined based on the concentration of GPEOR products (in mmol m^{-2} s^{-1}) and H_2 (in μmol m^{-2} s^{-1}), according to Eq. (9) [45].

$$r\left[\text{mol m}^{-2}\text{s}^{-1}\right] = \frac{\dot{n}}{A} \tag{9}$$

where $\dot{n}$ represents the generated product molar flow (in mol s^{-1}), and *A* is the geometric surface area of the photoanode (in m^2).

The FE, also referred to as current efficiency (in %), quantifies how efficiently the electric charge is used in a given electrochemical reaction.

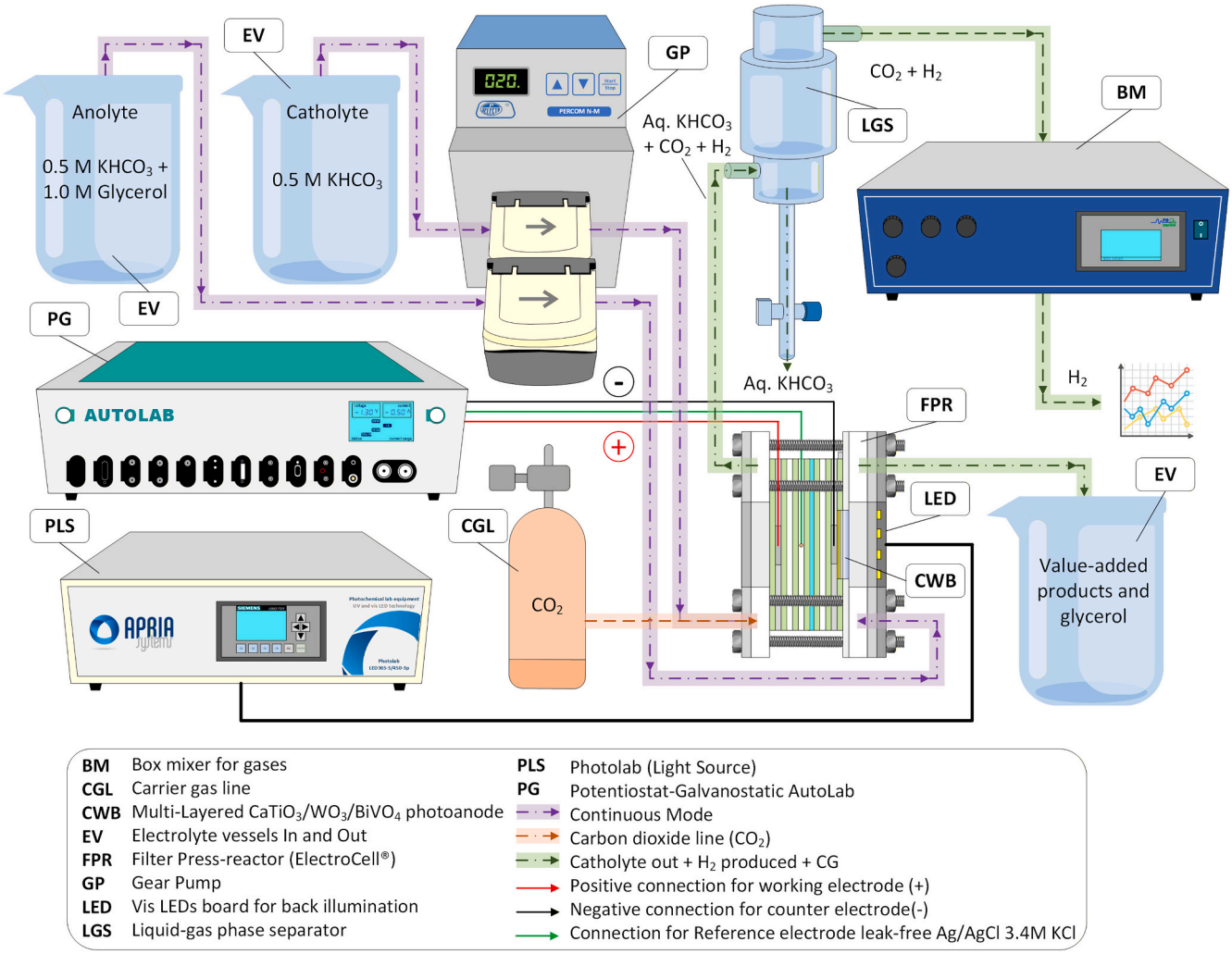

Fig. 1. Experimental setup for PEC trials.

It was defined as the ratio of the actual amount of product formed (from GPEOR and H_2) at an electrode to the theoretical amount expected based on the total charge passed through the system. Accordingly, FE was expressed as shown in Eq. (10) [46].

$$\mathrm{FE}\ [\%] = \frac{z\,F\,\dot{n}}{I} \times 100 \tag{10}$$

where z is the number of electrons involved in the reaction (DHA = 2; GEA = 4; $HCOO^-$ = 8/3; and H_2 = 2) [47,48], according to global Eqs. (11), (12), and (13), F is Faraday's constant (96,485C mol^{-1}), $\dot{n}$ is expressed in mol s^{-1}, and I is the total charge passed through the electrode (in A).

$$(\mathrm{DHA})\ C_3H_8O_3 + 2\,OH^- + 2\,h^+ \xrightarrow{h\nu \geq E_{bg}} C_3H_6O_3 + 4\,H_2O + 4\,e^- \tag{11}$$

$$(\mathrm{GEA})\ C_3H_8O_3 + 4\,OH^- \xrightarrow{h\nu \geq E_{bg}} C_3H_6O_4 + 4\,H_2O + 4\,e^- \tag{12}$$

$$(HCOO^-)\ C_3H_8O_3 + 11\,OH^- \xrightarrow{h\nu \geq E_{bg}} 3\,HCOO^- + 8\,H_2O + 8\,e^- \tag{13}$$

The S_i (in %) was used to evaluate the distribution of the oxidation products formed during GPEOR, as expressed in Eq. (14).

$$S_i[\%] = \frac{n_i}{\sum n_j} \times 100 \tag{14}$$

Where n_i is the amount of product (in mol), and $\sum n_j$ is the total amount of all quantified products (in mol). It has been calculated according to the method described in a previous work [49].

The E_{Con} refers to the amount of energy required to perform the water splitting for H_2 production, and it was calculated according to Eq. (15) [50].

$$E_{Con}\ \left[\mathrm{kWh\ kmol^{-1}}\right] = \frac{I\,E_{cell}}{\dot{n}} \tag{15}$$

where I is expressed in kA, E_{cell} is the absolute cell potential (in V), and $\dot{n}$ is expressed in kmol h^{-1}.

To calculate the CEE, it was first necessary to determine the potential of the Ag/AgCl reference electrode, which can be obtained with respect to the reversible hydrogen electrode (RHE), according to Eq. (16) [51].

$$E^0{}_{H^+/H_2}\ [\mathrm{V\ vs.RHE}] = E\ [\mathrm{V\ vs.Ag/AgCl}\ ] + E^0\ [\mathrm{V\ vs.Ag/AgCl}] + 0.059 \times \mathrm{pH} \tag{16}$$

where $E^0{}_{H^+/H_2}$ [V *vs.* RHE] is the overpotential required at the cathode to perform the HER (0 V *vs.* RHE), E [V *vs.* Ag/AgCl] is the measured potential of the reference electrode, and E^0 [V *vs.* Ag/AgCl] is the standard potential of the Ag/AgCl reference electrode in saturated KCl (+0.197 V *vs.* NHE at 25 °C). The solution had a pH of 8.7, and the potential *vs.* RHE linearly increased with pH, exhibiting a slope of 0.059 V pH^{-1} at 25 °C) [51–53].

The CEE represents the proportion of electrical energy effectively converted into H_2 gas during the PEC process, and was calculated according to Eq. (17) [54].

$$\mathrm{CEE}\ [\%] = \mathrm{FE} \times \frac{E_t}{E_c} \tag{17}$$

where FE is expressed in %, E_t is the theoretical potential needed for the formation of H_2 (in V *vs.* Ag/AgCl), and E_c is the cathodic applied potential (in V *vs.* Ag/AgCl).

3. Results and discussion

3.1. Characterization of CWB structure and morphology

The CWB films were analyzed using SEM-EDS, XRD, XPS, and BET techniques to investigate their surface morphology, chemical composition, crystallographic structure, optical properties, and textural characteristics. These combined analyses provided essential insights into the material properties that influence photocatalytic performance.

3.1.1. SEM-EDS analysis

Cross-sectional and surface analyses of the multilayer CWB photoanodes were performed using SEM-EDS to investigate morphological and compositional features before and after GPEOR. In the fresh photoanode (Fig. 2a and b), a well-defined multilayer architecture was observed, with each layer corresponding to a specific material. The elemental maps (Fig. S4) confirm the expected distribution: Bi and V were concentrated near the surface, W in the intermediate region, and Ca and Ti near the FTO substrate, consistent with the designed deposition sequence. After GPEOR (Fig. 2c and d), changes in the structural integrity and elemental distribution were evident. The Bi and V signals decreased significantly, suggesting partial dissolution or restructuring of the $BiVO_4$ layer. This apparent loss of Bi and V is consistent with the photocorrosion behavior of $BiVO_4$ under PEC operation. Several studies have shown that $BiVO_4$ photoanodes undergo partial dissolution of Bi and V species, accompanied by surface restructuring and material loss, which limits long-term stability under anodic bias and illumination [55,56]. Additionally, the presence of K in FU-Z2 of used samples is likely related to residual K^+ from the electrolyte ($KHCO_3$), which tends to adsorb or infiltrate into the porous region.

The evolution of the layer thickness was assessed from fractured cross-sections of the CWB photoanodes. In the fresh photoanode, the $BiVO_4$ exhibited an average thickness of 17.6 ± 1.6 μm, followed by 3.6 ± 1.2 μm for the WO_3 intermediate layer, and 6.0 ± 1.3 μm for the $CaTiO_3$ base layer deposited over FTO. After GPEOR, the $BiVO_4$ layer showed a slight but consistent reduction in thickness to 14.6 ± 2.0 μm, indicating partial dissolution or structural compaction. The other layers remained stable with 2.1 ± 0.6 μm (WO_3) and 5.8 ± 0.7 μm ($CaTiO_3$).

The quantitative EDS data (Table 1) further supported these observations and were consistent with the thickness measurements. In the fresh photoanode, Bi and V were prominently detected in zone FN-Z1 (surface), while W (FN-Z3) and Ti (FN-Z4) dominate in the middle and deeper regions, respectively. In contrast, some zones exhibited high levels of F (57.1%) and C (32.3%), along with smaller amounts of O and S. This composition strongly suggests the presence of the Nafion®, a fluorinated polymer containing $–CF_2/–CF_3$ groups, sulfonic acid groups ($-SO_3H$), and carbon-fluorinated backbone [57]. After GPEOR, a noticeable drop in Bi and V content was observed in FU-Z1, suggesting partial surface modification of the $BiVO_4$. The surface composition was modified under operating conditions, reflecting typical changes expected in photoactive materials exposed to electrolyte environments. Despite these modifications, the multilayer structure remained largely preserved, supporting its applicability in sustained PEC processes.

Top-view SEM images (Fig. S5) and BSE-mode micrographs (Fig. S6) highlight the structural and compositional evolution of the CWB photoanode surface before and after GPEOR. The fresh photoanode exhibited smooth, uniform morphology, with a continuous coating indicative of a well-distributed active layer. After the operation, the surface became slightly rougher, with localized accumulation of particulates, as seen in Fig. S5f, where the intermediate layer of WO_3 appeared. EDS analysis (Fig. S7, Table S2) confirmed the dominant presence of Bi and V on top of the photoanode (Z1), consistent with the $BiVO_4$ layer. In peripheral zones (Z2), high F and C content confirmed the presence of the Nafion ionomer. Post-GPEOR spectra show that the Nafion layer was largely retained, though with a slight decrease in F signal and increased detection of K and S, likely due to electrolyte ($KHCO_3$) interaction. The emergence of the S signal may also be attributed to electrochemical swelling and reorganization of the ionomer under operation, which can bring $-SO_3H$ groups closer to the surface. Additionally, partial degradation of Nafion under anodic potentials and local pH fluctuations may generate surface-bound sulfonate or sulfate fragments, contributing to the sulfur enrichment detectable by

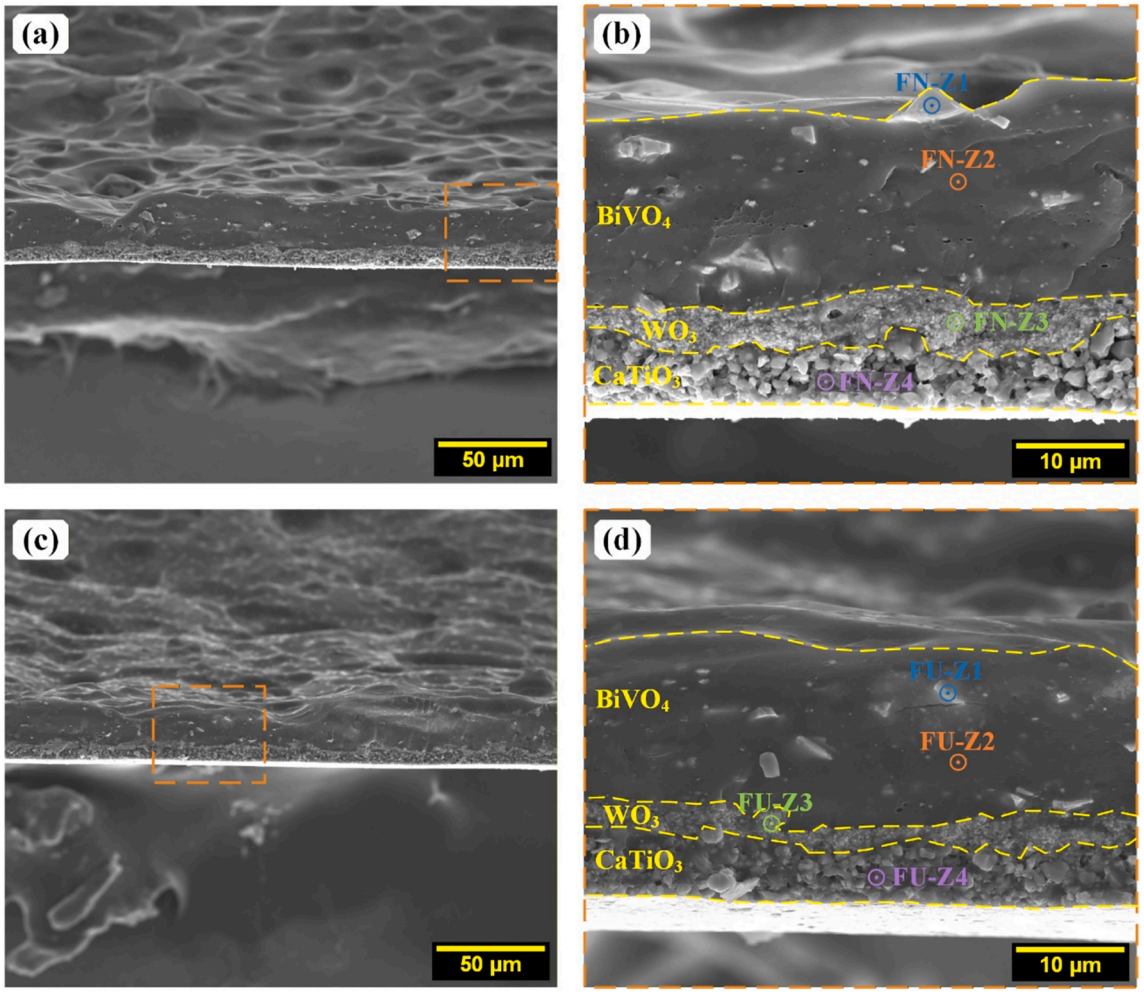

Fig. 2. Cross-sectional SEM images (ETD, SE mode) of the multilayer CWB photoanode: (a,b) fresh and (c,d) after GPEOR. FN: fresh non-fractured; FU: used fractured; Z1–Z4: zones.

Table 1
Elemental composition (at.%) of the fractured CWB photoanode before (FN) and after use (FU) in different zones.

Sample	C	O	F	S	W	Bi	V	Ca	Ti	K
FN-Z1	7.8	25.4	9.4	3.0	0.6	24.7	29.1	0	0	0
FN-Z2	26.4	2.8	55.5	3.6	0.1	0.5	0.8	0	0	10.4
FN-Z3	10.5	30.1	1.9	0.3	90.3	0	0	0	0	2.9
FN-Z4	3.7	23.7	6.5	0.4	0.4	0.1	0	30.9	33.5	0.8
FU-Z1	17.0	18.4	38.5	1.7	2.7	7.8	7.9	0	0	6.0
FU-Z2	26.9	3.4	54.2	4.2	0.7	0.7	1.0	0	0	9.0
FU-Z3	9.0	14.3	1.7	2.3	53.4	0	0	0	0	11.4
FU-Z4	6.2	31.4	10.5	0.4	0.6	0	0	24.2	24.7	2.0

EDS. Importantly, although Bi and V signals were still detected after operation, their reduced intensity is consistent with the compositional changes discussed above, indicating partial dissolution and surface modification of the $BiVO_4$ layer.

3.1.2. XRD analysis

The crystallographic structure of the CWB photoanode before and after use is presented in Fig. 3,where the experimental pattern is compared with the corresponding International Centre for Diffraction Data (ICDD) reference patterns of $CaTiO_3$, WO_3, and $BiVO_4$. The microstructural parameters extracted from XRD analysis are summarized in Table S3.

Both fresh and used photoanodes exhibit well-defined diffraction peaks that can be indexed to orthorhombic $CaTiO_3$, monoclinic WO_3, and monoclinic $BiVO_4$, confirming the successful incorporation of all components in the multilayer structure. Characteristics reflections of $CaTiO_3$ are observed at $2\theta = 23.2°$ (101), $2\theta = 33.1°$ (121), and $2\theta = 47.5°$ (202) [58], while WO_3 is identified by peaks at (020) at $2\theta = 23.6°$, (200) at $2\theta = 24.3°$, and (022) at $2\theta = 34.1°$ [59,60]. The presence of monoclinic $BiVO_4$, corresponding to its most photoactive phase, is confirmed by reflections $2\theta = 19.0°$ (011), $2\theta = 29.0°$ (121), and $2\theta = 30.5°$ (040) [61,62]. The comparison between fresh and used samples indicates that the main diffraction peaks remain essentially unchanged after GPEOR, confirming that the crystalline structure of the photoanode is preserved and supporting its structural stability during operation. Although slight variations in peak intensity are observed, no evident new crystalline peaks appear after reaction, suggesting that these changes are more likely associated with surface modification, partial

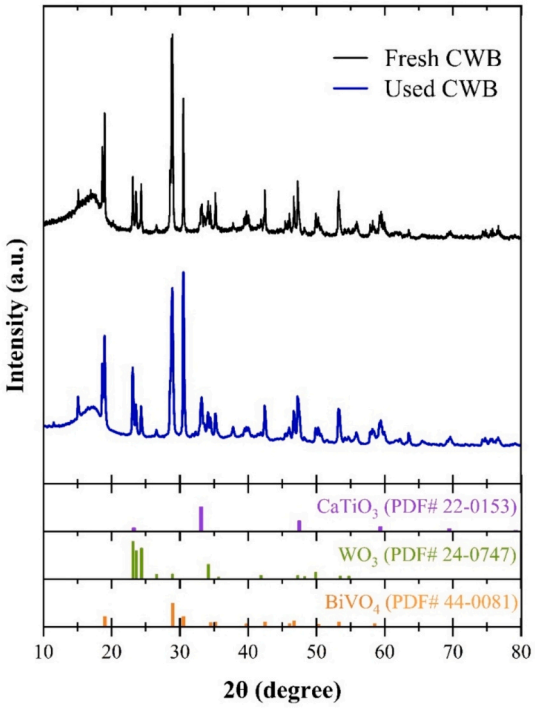

Fig. 3. XRD pattern of the multilayer CWB photoanode before and after GPEOR.

restructuring, or differences in the relative contribution of the outer layers rather than the formation of new crystalline phases. This interpretation is consistent with the SEM-EDS results, which indicate changes mainly at the surface of the $BiVO_4$-rich outer region. Regarding the unassigned peaks in the 2θ range of 17–80°, these features are mainly due to overlapping, weaker reflections of the constituent crystalline phases, along with minor background contributions from the substrate. In addition, the broad feature observed around $2\theta \approx 15–17°$ is assigned to the amorphous contribution of the Nafion binder, consistent with its semicrystalline structure reported in the literature [40].

Beyond phase identification, the microstructural parameters extracted from XRD (Table 2) provide further insight into the role of each layer in the CWB photoanode. $BiVO_4$ positioned at the surface exhibited the largest D (108.9 ± 9.4 nm) and lowest ε and δ, indicating a highly ordered structure favorable for charge separation. The intermediate WO_3 layer showed smaller crystallites (39.2 ± 4.1 nm) and the highest ε, which may promote charge transport and enhance surface reactivity. $CaTiO_3$, as the bottom layer, presented intermediate values, acting as a stable and conductive base.

3.1.3. XPS analysis

Further evidence of the electronic structure and surface stoichiometry of the multilayer CWB photoanode was obtained by XPS from the survey of each oxide (Fig. S8). For all samples, the C 1 s peak centered at 285.0 eV (Fig. S9a) originated from adventitious hydrocarbons and was used as the internal binding-energy reference. High-resolution O 1 s spectra (Fig. S9b) were dominated by the lattice-oxygen component at 529.5 eV and 530.7 eV, while a higher binding energy shoulder at 531.1 eV and 531.8 eV can be assigned to surface hydroxyls and chemisorbed oxygen species. This is lined with previous literature, with peaks at 530.5 eV and 532.0 eV, respectively, characteristic of stable metal-oxide photoanodes [30,49]. The $CaTiO_3$ layer exhibited Ca $2p_{3/2}$ (346.7 eV) and Ca $2p_{1/2}$ (350.3 eV) peaks (Fig. 4a), which are characteristic of Ca^{2+} species [63]. Ti $2p_{3/2}$ and Ti $2p_{1/2}$ signals at 458.4 eV and 464.1 eV (Fig. 4b) confirm the exclusive presence of Ti^{4+}, with no discernible Ti^{3+} component, such as that observed in mixed-valence perovskites [64]. Values obtained from W 4f (Fig. 4c) at 35.9 eV ($4f_{7/2}$) and 38.1 eV ($4f_{5/2}$) can be assigned to W^{6+} according to the literature [65]. V $2p_{3/2}$ was centered at 517.3 eV with a minor shoulder at 524.8 eV (Fig. 4d), indicating a small fraction of V^{4+} sites. Such undercoordinated V atoms can facilitate interfacial charge transfer without compromising structural integrity. Ultimately, the $BiVO_4$ layer (Fig. 4e) showed Bi $4f_{7/2}$ and Bi $4f_{5/2}$ peaks at 159.7 eV and 165.0 eV, respectively, confirming the presence of Bi^{3+} in the outermost layer [66]. Overall, the XPS results confirm that all components retain their expected oxidation states. Slight variations in binding energy suggest interfacial electronic interactions between $CaTiO_3$, WO_3, and $BiVO_4$, promoting improved charge separation and transfer, consistent with enhanced PEC performance.

The surface atomic compositions obtained from wide-scan XPS (Table 3) confirm the presence of the expected elements in each individual oxide. Notably, the $CaTiO_3$ film showed an approximated Ca/Ti ratio of 2.0, suggesting slight Ti surface depletion or Ca surface enrichment, a common feature in perovskite oxides [63]. The WO_3 layer presented a high O/W ratio (approx. 6.4), indicating a hydroxylated surface. Finally, the $BiVO_4$ layer exhibited significant deviation from stoichiometry (Bi/V: 2.6), indicating pronounced surface enrichment [67]. These features can enhance surface reactivity and influence glycerol adsorption and reaction pathways. Hydroxylated oxygen species identified in the O 1 s spectra may promote adsorption configurations that favor selective oxidation of the secondary –OH group. Therefore, it can preserve the C—C backbone and lead to the formation of DHA. Moreover, the Bi-enriched surface may modify the distribution and nature of active sites, contributing to the stabilization of intermediates associated with C_3 products [68]. In combination with the efficient charge separation promoted by the CWB heterostructure, these effects can limit overoxidation and suppress C—C bond cleavage, thereby favoring partial oxidation pathways.

3.1.4. BET analysis

Nitrogen adsorption-desorption isotherms for $CaTiO_3$, WO_3, and $BiVO_4$ are shown in Fig. S10. All materials exhibited type IV isotherms, according to IUPAC classification, which is characteristic of mesoporous structures [69]. However, the specific surface area values are relatively low and fall within a narrow range, limiting a detailed comparative analysis between samples. Overall, similar textural properties were observed among the oxides. The corresponding BET surface area and pore volume values (Table S4) show that WO_3 presents slightly higher values, followed by $CaTiO_3$, while $BiVO_4$ exhibits the lowest values. These low surface area values are consistent with those typically reported for oxide materials, which generally fall in the range of 2–10 $m^2 g^{-1}$ [70].

Table 2
Crystallographic and microstructural parameters of CWB photoanode components after GPEOR.

Avg. structural parameter	$CaTiO_3$	WO_3	$BiVO_4$	Relevant properties
D (nm)	49.3 ± 8.6	39.2 ± 4.1	108.9 ± 9.4	$BiVO_4$ has larger and more well-formed crystallites
ε	(2.4 ± 0.3) × 10^{-3}	(3.5 ± 0.5) × 10^{-3}	(1.2 ± 0.2) × 10^{-3}	WO_3 is more strained; $BiVO_4$ is the most ordered
δ (lines m^{-2})	(7.5 ± 3.2) × 10^{-4}	(1.0 ± 0.3) × 10^{-3}	(1.6 ± 0.7) × 10^{-4}	$BiVO_4$ exhibits the "cleanest" crystallite structure
d_{hkl} (nm)	0.21 ± 0.04	0.26 ± 0.02	0.24 ± 0.02	–

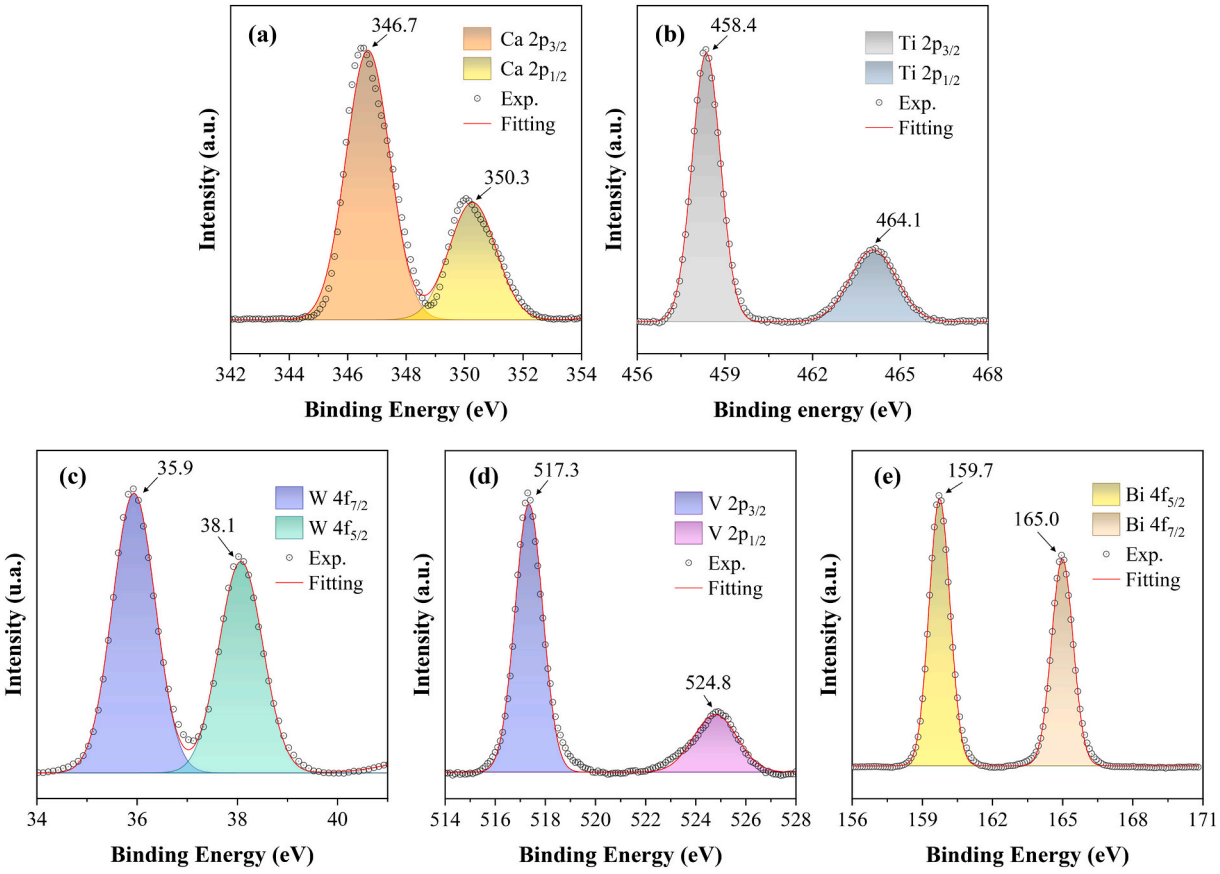

Fig. 4. High-resolution XPS spectra of the multilayer CWB photoanode before GPEOR: (a) Ca 2p, and (b)Ti 2p ($CaTiO_3$ layer), and (c) W 4f (WO_3 layer), and (d) V 2p, and (e) Bi 4f ($BiVO_4$ layer).

Table 3
Surface atomic composition (at.%) of the individual oxide layers in the CWB photoanode before GPEOR.

Sample	C	O	Ca	Ti	W	V	Bi
$CaTiO_3$	24.6	52.4	15.5	7.6	0	0	0
WO_3	20.1	69.1	0	0	10.8	0	0
$BiVO_4$	42.7	11.7	0	0	0	12.8	32.8

3.2. GPEOR – Photoanode characterization and efficiency

3.2.1. PEC response of the CWB photoanode

The LSV curves of the CWB photoanode, shown in Fig. 5a, reveal a higher photocurrent under illumination compared to dark conditions, indicating a clear photoresponse. In this configuration, the measured current reflects the cathodic HER response, which is enhanced by the extra photogenerated electrons supplied by the illuminated photoanode. The onset potential was observed at approximately −0.8 V *vs.* Ag/AgCl, demonstrating that visible light effectively drives the photo-electrooxidation process, especially at more negative potentials. Although no experiments were conducted in acidic media in this work, the literature generally indicates that GPEOR presents a significantly higher oxidation *j* at low overpotentials in alkaline media relative to acidic media [71], justifying the use of alkaline conditions in this study.

The LSV results were further confirmed by CP measurements at various *j* (Fig. 5b), which revealed that the photoanode maintained stable performance at lower *j*. For instance, at −10 mA cm^{-2}, the photoanode exhibited significantly improved stability, sustaining consistent performance over an extended period of 3600 s. A *j* of −200 mA cm^{-2} corresponded to an impressive potential of −1.45 V *vs.* Ag/AgCl. In comparison, our previously reported $CaTiO_3/BiVO_4$ photoanode achieved a *j* of only −71 mA cm^{-2} at a more negative potential of −1.8 V *vs.* Ag/AgCl [40]. This suggests that while higher *j* can deliver greater photocurrent, they may also accelerate photoanode degradation, highlighting a trade-off between PEC performance and long-term stability. Under 1 sun illumination, $BiVO_4$ photoanodes are limited to photocurrent densities of ~7.5 mA cm^{-2}, whereas the current densities applied in this work (10–200 mA cm^{-2}) significantly exceed this range [72,73]. This indicates that illumination primarily reduces the required external bias rather than sustaining the total current. This behavior explains the small differences observed between light and dark conditions. Importantly, this work demonstrates a photo-assisted system operating at industrially relevant current densities, where solar input contributes to lowering the overall energy demand and enables future coupling with value-added cathodic reactions such as CO_2RR.

EIS measurements (Fig. 5c) revealed a significant decrease in charge transfer resistance under irradiation, both in the absence and presence of glycerol, indicating enhanced charge separation and electron transfer. For these measurements, the electrode configuration was adjusted to probe the photoanode properties, enabling direct assessment of interfacial charge transfer. The Nyquist plots display a larger semicircle radius in the presence of glycerol, reflecting an increase in charge transfer resistance (R_{ct}), as can be seen in Table S5. Specifically, the R_{ct} at the CWB photoanode/electrolyte interface was 14.8 Ω in aqueous 0.5 M $KHCO_3$ solution under irradiation, indicating a better charge transfer. When 1.0 M glycerol was added to the anolyte, the R_{ct} increased to 17.1 Ω, likely due to the higher viscosity of the solution in the presence of glycerol, which can hinder ion transport between the bulk solution and the catalyst surface [74]. For comparison, the bare FTO electrode exhibited a significantly smaller semicircle, indicating its minimal electrochemical contribution and confirming that the observed response

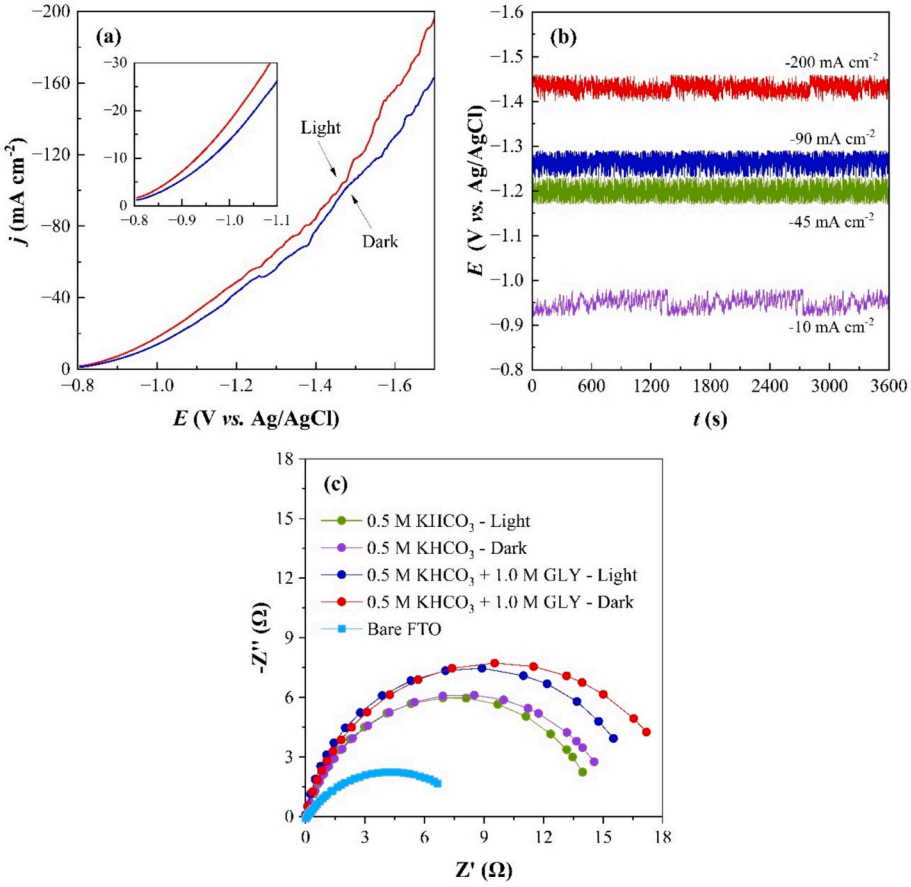

Fig. 5. CWB photoanode PEC response: (a) LSV curves at a scan rate of 50 mV s^{-1} under light (100 mW cm^{-2}) and dark conditions, (b) CP results for different fixed *j* under illumination, (c) Nyquist plots from EIS analysis at 0.8 V (*vs.* Ag/AgCl) over 10^{-1} to 10^{5} Hz under light and dark conditions using different anolytes. Measurements were conducted in 0.5 M $KHCO_3$.

is dominated by the multilayer photoanode. This behavior is consistent with previous EIS studies on similar multilayer systems, which reported reduced charge-transfer resistance and improved interfacial charge transport [41]. For instance, higher $BiVO_4$ loadings (80:20 $BiVO_4$:WO_3) under visible light irradiation have been reported to yield lower charge transfer resistance and improved electron transfer due to efficient e^-_{CB}/h^+_{VB} separation [41]. Remarkably, the CWB photoanode exhibited charge transfer resistance values approximately 80-fold lower than those typically reported in the literature [75]. In addition to the new material, this improvement can be attributed to the use of an electrochemical flow

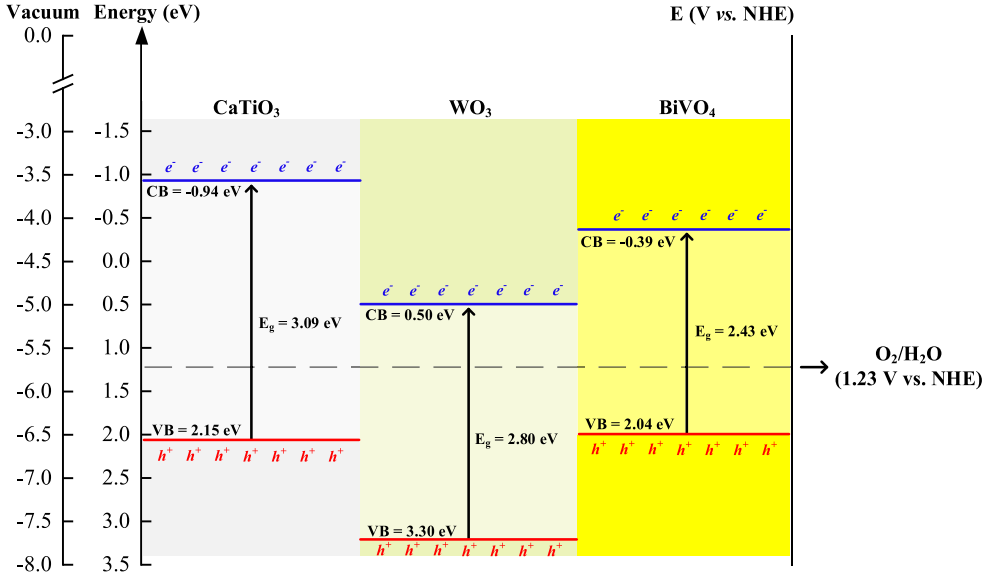

Fig. 6. Schematic band diagram of the CWB photoanode, showing VB and CB energy levels (in eV). Adapted from Nasir et al. [80], Radha et al. [81], and Passi & Pal [89].

cell, which enhances electrolyte circulation, reduces the diffusion boundary layer, and improves mass and charge transfer [76]. As a result, resistance is minimized and the CWB photoanode/electrolyte interface is optimized (Fig. S11). This efficient electron generation also highlights the system's potential for coupling with cathodic CO_2RR.

3.2.2. Charge transfer mechanisms in the CWB photoanode

The proposed band alignment for the multilayer CWB photoanode was inferred from literature-reported bandgap values and band-edge positions for the individual semiconductors ($CaTiO_3$, WO_3, and $BiVO_4$), together with previous studies on related heterostructured systems. $CaTiO_3$ was the bottom layer, deposited directly onto the FTO substrate, followed by WO_3 and $BiVO_4$, the intermediate and top layers, respectively. This multilayered configuration can optimize the separation and transport of photogenerated charges, leveraging the complementary properties of each material. Reported bandgap values (~3.1–3.6 eV for $CaTiO_3$, 2.8–2.9 eV for WO_3, and ~2.4 eV for $BiVO_4$) support their complementary properties and were used, together with literature band-edge positions, to construct the band diagram (Fig. 6) [40,41]. Importantly, it should be regarded as a schematic representation intended to describe the expected charge-transfer pathway within the multilayer architecture, rather than as an experimentally determined absolute band structure. The improved performance of the CWB photoanode can be mainly attributed to enhanced charge separation rather than increased light absorption. $BiVO_4$ acts as the visible-light absorber, while the $WO_3/BiVO_4$ type-II heterojunction promotes electron transfer and suppresses recombination [77]. The $CaTiO_3$ layer further contributes as an electron collector, reinforcing charge separation across the multilayer structure [78].

The multilayered CWB heterostructure enhances charge separation *via* type-II band alignment, increasing hole availability for GPEOR. The type-II band alignment in the $WO_3/BiVO_4$ heterojunction promotes electron transfer from $BiVO_4$ to WO_3, while holes remain in $BiVO_4$, resulting in effective spatial charge separation and reduced recombination [79]. This enhanced charge separation increases the availability of photogenerated holes at the semiconductor/electrolyte interface, which are directly involved in glycerol oxidation. Replacing the energy-intensive OER with glycerol oxidation reduces energy consumption while enabling the production of value-added chemicals. This co-valorization strategy also allows coupling with cathodic reactions (*e.g.*, H_2 evolution or CO_2RR), improving overall system efficiency and sustainability.

According to literature-reported band-edge positions, the conduction band of $BiVO_4$ is more negative than that of WO_3, favoring electron transfer from $BiVO_4$ to WO_3 and promoting spatial charge separation within the heterojunction [41,80,81]. Moreover, WO_3 exhibited significantly higher electron mobility (12 $cm^2\ V^{-1}\ s^{-1}$) compared to $BiVO_4$ (0.01 $cm^2\ V^{-1}\ s^{-1}$) [38,39]. This property facilitates electron transport across the heterostructure and justifies the placement of WO_3 between $BiVO_4$ and $CaTiO_3$. Acting as a bridge layer, WO_3 promotes efficient electron extraction, while $BiVO_4$, with its narrower bandgap, enables effective generation of e^-_{CB}/h^+_{VB} pairs. The $BiVO_4$ layer thickness (~17.6 μm) exceeds the typical hole diffusion length (<70 nm), which can limit charge transport and increase recombination [82]. Although optimized photoanodes typically use thinner layers (~100–200 nm) [83], the micrometric particle structure in this work reduces effective transport distances and facilitates charge percolation, while $WO_3/BiVO_4$ heterojunction and the applied bias enhance charge separation and transport.

EIS analysis confirms that WO_3 significantly influenced both the capacitive and transport properties of the $WO_3/BiVO_4$ heterojunction [84]. The interface forms a type-II (n–n) heterojunction with a staggered band alignment. This staggered band alignment is expected to promote charge separation by favoring electron migration toward WO_3 and hole accumulation at the $BiVO_4$ surface [85,86]. As a result, charge separation is further enhanced. Considering the wide bandgap nature of $CaTiO_3$ and literature-reported band energetics, $CaTiO_3$ is more likely to contribute as an interfacial layer that assists charge redistribution and structural stabilization within the multilayer architecture, rather than acting as the primary electron transport pathway [87,88]. At lower *j*, these transport limitations become less pronounced, as observed in CP analysis. The reduced rate of charge generation is better aligned with the system's transport dynamics. This minimizes recombination losses and ensures stable operating performance. Although $CaTiO_3$ is in contact with the FTO substrate, it does not act as a conventional electron transport layer. Instead, it mainly contributes to structural stability and interfacial charge modulation, while electron transport is primarily governed by the $WO_3/BiVO_4$ interface, differing from our previous interpretation[40].

The performance of the CWB photoanode is supported by the experimental results. Further theoretical studies, such as Density Functional Theory (DFT) calculations, could provide deeper insight into interfacial charge transfer, adsorption energetics, and reaction pathways within the developed photoelectrode [90].

3.2.3. GPEOR

Table 4 presents a detailed comparison of studies on GPEOR reported in the literature using various photoanodes, highlighting both their experimental conditions and key outcomes. Most WO_3- and $BiVO_4$-based photoanodes operate under strongly acidic conditions (pH $\leq$ 2.0), whereas this study adopted a moderate alkaline pH of 8.7. This shift can not only mitigate corrosion issues and support more sustainable reaction conditions but also stabilize reactive intermediates, driving the reaction toward the selective formation of C_3 products such as DHA and GEA.

It should be noted that most studies summarized in Table 4 were conducted in conventional batch PEC cells, where the electrolyte remains in contact with the photoanode for an extended period and products accumulate in the reaction medium. In contrast, the GPEOR in this work was carried out in continuous, single-pass operation, which alters mass transfer conditions, residence time, and product distribution. Therefore, both selectivity and FE may differ when compared with batch PEC systems.

The main products were C_3 compounds, including DHA and GEA, along with the C_1 product (FA)/$HCOO^-$ (see Fig. S12 for the proposed oxidation pathways), in agreement with the literature. Insights into the oxidation pathways of the GPEOR are provided in the Supporting Information. The results in Fig. 7a indicate high FE and production rates, particularly at lower *j* and under back-illumination. The FE for DHA, GEA, and $HCOO^-$ at 90 mA cm^{-2} at the cathode was approximately 3%, 8%, and 2%, respectively. These values increased to about 24%, 21% and 18%, respectively, as the *j* decreased to 10 mA cm^{-2}. The FE toward quantified glycerol oxidation products (~64%) indicates that part of the charge was consumed by parallel reaction pathways, as commonly reported in glycerol (photo)electrooxidation systems. The remaining unaccounted charge can be attributed to parallel processes, including the OER, over-oxidation of glycerol and its intermediates, and partial mineralization to CO_2. The formation of CO_2 during glycerol oxidation has been experimentally demonstrated, even at relatively low potentials, with a substantial fraction remaining dissolved as carbonate species in alkaline media [91]. In addition, the complex GOR network may lead to the formation of undetected intermediates or products, thereby contributing to the incomplete balance.

Furthermore, at $j = 10$ mA cm^{-2}, a more favorable balance between charge utilization, selectivity, and photoanode stability was achieved, which is particularly relevant for PEC systems. The effect of *j* on product distribution and process efficiency was also evaluated up to 90 mA cm^{-2}, in line with previous studies on continuous-flow glycerol electrooxidation systems, where higher current densities (up to 200 mA cm^{-2}) are typically explored [92]. However, such conditions often involve trade-offs between production rate, selectivity, and stability, especially in PEC systems limited by photon flux [24]. The CWB photoanode under light irradiation formed valuable glycerol-derived products with a product rate of 124 ± 6 μmol $m^{-2}\ s^{-1}$ for DHA, 55 ± 2 μmol

Table 4
Comparative analysis of photoanode materials and their photoelectrochemical performance for glycerol oxidation reported in the literature.

Photoanode	Deposition technique [a]	Cathode	System operation	Light intensity (light source)	Electrolyte (pH) [b]	j (mA cm^{-2})	Main product(s) [c]	Selectivity (%)	FE (%)	Ref.
$CaTiO_3/WO_3/BiVO_4$	SYC	Platinized titanium plate	Continuous	100 mW cm^{-2} (visible light)	0.5 M $KHCO_3$ + 1.0 M GLY (pH = 8.7)	−10	DHA + GEA	71	45	This work
$W:BiVO_4$	ED	Pt mesh	Batch	100 mW cm^{-2} (visible light)	0.5 M Na_2SO_4 + 0.1 M GLY (pH = 7.0)	~2.0	FA/ $HCOO^-$	n.a.	70	[95]
$NiO_x(OH)_y/W:BiVO_4$	ED	Pt mesh	Batch	100 mW cm^{-2} (visible light)	0.5 M KBi + 0.1 M GLY (pH = 9.3)	~2.9	FA/ $HCOO^-$	n.a.	~45	[95]
$BiVO_4$	*SIC*	Pt mesh	Batch	100 mW cm^{-2} (UV–Vis)	0.1 M NaBi +0.1 M GLY (pH = 9.4)	0.3	FA/ $HCOO^-$	85	n.a.	[30]
WO_3	HSFC	Pt (20% wt.)/C	Semi-continuous	41 mW cm^{-2} (UV light)	Pure water +0.1 M GLY (pH = 5.5)	~2.1	GLAD	26	~34	[31]
m-H-WO_3/TiO_2	SAHM	Pt wire	Batch	100 mW cm^{-2} (UV–Vis)	0.5 M Na_2SO_4 + 0.1 M NaBi +0.1 M GLY (pH = 6.0)	~2.9	GLAD + DHA	85	70	[96]
(010)-$BiVO_4$	*SIC*	Pt mesh	Batch	100 mW cm^{-2} (UV–Vis)	0.1 M NaBi +0.1 M GLY (pH = 2)†	1.4	DHA	~60	n.a.	[97]
$BiVO_4$	ED	Pt wire	Batch	100 mW cm^{-2} (visible light)	0.5 M $NaNO_3$ + 0.1 M GLY (pH = 2)	2.7	GCAD	55	n.a.	[98]
$WO_3/BiVO_4/Bi$	SD	Pt foil	Batch	100 mW cm^{-2} (UV–Vis)	0.5 M Na_2SO_4 + 0.1 M GLY (pH = 2)†	3.6	DHA	~61	~35	[66]
$WO_3/BiVO_4$	SD	Pt foil	Batch	100 mW cm^{-2} (UV–Vis)	0.5 M Na_2SO_4 + 0.1 M GLY (pH = 2)†	~2.3	DHA	~53	~31	[66]
WO_3	SD	Pt foil	Batch	100 mW cm^{-2} (UV–Vis)	0.5 M Na_2SO_4 + 0.1 M GLY (pH = 2)†	1.6	DHA	~38	~27	[66]
(202)-WO_3	HSFC	Pt wire	Batch	100 mW cm^{-2} (UV–Vis)	0.1 M Na_2SO_4 + 1 M GLY (pH = 2.0)	~3.3	GLAD	80	75	[99]
$Ta:BiVO_4/BiVO_4/WO_3$	*SIC*	Pt wire	Batch	100 mW cm^{-2} (visible light)	0.025 M H_2SO_4 + 1.0 M GLY (pH =1.6)*	~2.7	DHA	99	61	[100]
$TaO_x/BiVO_4/WO_3$	*SIC*	Pt wire	Batch	100 mW cm^{-2} (visible light)	0.025 M H_2SO_4 + 1.0 M GLY (pH = 1.6)*	~1.1	DHA	n.a.	53	[100]
WO_3	HSFC	Pt wire	Batch	n.a.	0.5 M Na_2SO_4 + 0.1 M GLY (pH = 6.0)	~0.6	GLAD	~63	~41	[49]

n.a. – not available.
[a] Deposition technique: spin-coating (*SIC*), electrodeposition (ED), solution deposition (SD), seed-assisted hydrothermal method (SAHM), hydrothermal synthesis followed by calcination (HSFC), spray-coating (SYC);
[b] Electrolyte: glycerol (GLY), sodium borate buffer (NaBi), potassium borate buffer (KBi), sulfuric acid (H_2SO_4), sodium sulfate (Na_2SO_4), sodium nitrate ($NaNO_3$);
[c] Main product(s): Formic acid (FA), dihydroxyacetone (DHA), glyceraldehyde (GLAD), glycolaldehyde (GCAD);
* pH was calculated using the equation: pH = − log [H^+];
† pH was adjusted using a 0.5 M solution of H_2SO_4 solution;

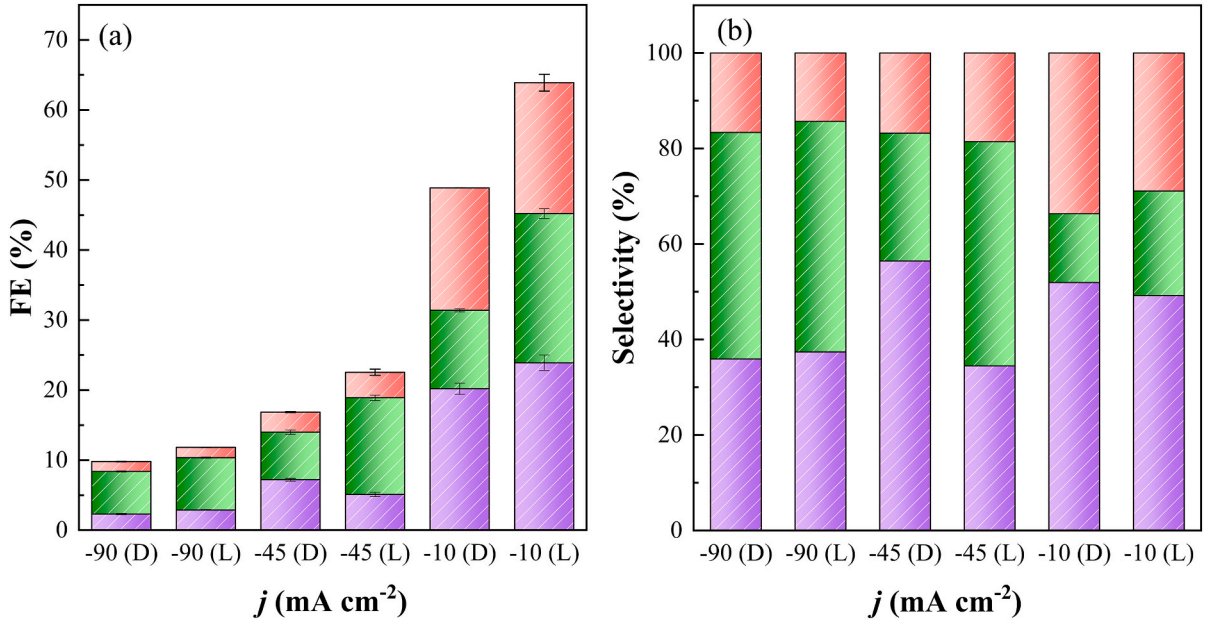

Fig. 7. (a) Faradaic efficiency, and (b) product selectivity at various j under back-illumination (100 mW cm^{-2}) – L and dark conditions – D. Legend: DHA, GEA, $HCOO^-$.

m^{-2} s^{-1} for GEA, and 73 ± 5 μmol m^{-2} s^{-1} for $HCOO^-$, resulting in a total FE of 64%. Conversely, in the dark, the CWB photoanode produced 105 ± 4 μmol m^{-2} s^{-1} of DHA, 29 ± 1 μmol m^{-2} s^{-1} of GEA, and 67.9 ± 0.1 μmol m^{-2} s^{-1} of $HCOO^-$, corresponding to a total FE of 49%.

The S_i (Fig. 7b) indicates that lower *j* favors the formation of C_3 products (DHA and GEA), whereas higher *j* promotes a shift toward C_1 products such as $HCOO^-$, reflecting enhanced C—C bond cleavage and deeper oxidation pathways. This behavior is consistent with previous studies, where stronger oxidative conditions favor formate production due to the increased availability of highly oxidizing surface intermediates that accelerate consecutive oxidation steps [93]. In contrast, milder conditions (*e.g.*, lower *j* and moderate pH) promote the accumulation of partially oxidized C_3 compounds by limiting overoxidation and preserving the C_3 backbone. Therefore, the higher selectivity toward DHA and GEA at −10 mA cm^{-2} highlights a more controlled oxidation regime, which is particularly advantageous for glycerol valorization. This trend is further supported by recent studies reporting high selectivity toward C_3 intermediates under controlled conditions, where suppressing C—C bond cleavage and limiting overoxidation are essential to preserve C_3 valuable products. Notably, S_i above 80% toward C_3 products has been achieved by stabilizing early-stage intermediates and promoting their desorption before further oxidation can occur [94].

When compared with other single, modified, and multilayered photoanodes reported in the literature, including $NiO_x(OH)_y$/W:$BiVO_4$ (23 μmol m^{-2} s^{-1}),W:$BiVO_4$ (19 μmol m^{-2} s^{-1}), pl-H-WO_3 (4 μmol m^{-2} s^{-1}), and m-H-WO_3/TiO_2 (26 μmol m^{-2} s^{-1}) at 1.2 V *vs* RHE [95,96], the DHA production rate of the CWB photoanode was 5–31 times higher. Additionally, the potential found in the present work is −0.95 V *vs.* Ag/AgCl (−0.24 V *vs.* RHE). The use of negative potential at the cathode further promoted reduction reactions, contributing to the overall system performance. The enhanced production rate of glycerol oxidation products in the CWB photoanode can be attributed to the synergistic effects of its multilayered architecture. This interpretation is consistent with previous studies from our group, where $BiVO_4$/WO_3 heterostructures showed improved charge separation and reduced recombination compared to single-component systems [41]. Also, $CaTiO_3$-based multilayer configurations were found to enhance charge transport and electrode stability [40]. Furthermore, optimized CWB systems have demonstrated superior performance under similar fabrication strategies, confirming the beneficial interfacial interactions between layers [78]. In this context, the $CaTiO_3$ layer contributed to improved electrochemical stability, WO_3 facilitated charge transport, and $BiVO_4$ enhanced visible-light absorption, collectively leading to the observed performance enhancement.

3.3. Hydrogen production

The photoactive properties of the novel multilayered heterostructured photoanode enhanced H_2 production at the cathode. Recent studies have demonstrated that coupling HER with the electrooxidation of biomass-derived molecules is an effective strategy to overcome the limitations of conventional water splitting. Replacing the OER with organic oxidation reactions significantly reduces the required cell potential while simultaneously producing value-added chemicals. For example, systems based on heterostructured catalysts, such as RuO_2-modified NiS_2 or Pt-based heterojunctions, have shown that biomass oxidation can lower the overall splitting voltage to values close to ~1.1–1.5 V while maintaining high H_2 production efficiency. Similarly, glycerol electrooxidation has been identified as a promising alternative anodic reaction, enabling lower overpotentials and improved energy efficiency in H_2 production systems[101]. These studies highlight the importance of catalyst design and anodic reaction engineering in enhancing H_2 evolution.

Upon light excitation, glycerol oxidation occurred at the photoanode, producing H^+ that selectively transited through the PEM, minimizing interference from undesired chemical species and ensuring efficient charge balance in the system. Concurrently, electrons generated in the CWB layers were efficiently directed toward the cathode through an external circuit, driving the reduction of water and H_2 evolution. Fig. 8 shows the H_2 production rate (r_{H_2}) at different *j* and under illumination conditions, along with the respective E_{Con} and CEE values. The H_2 generation was higher for higher *j*, with a maximum r_{H_2} of 3458 ± 18 μmol m^{-2} s^{-1} observed at −90 mA cm^{-2} under light conditions. Operation in the dark resulted in lower r_{H_2}, particularly at a *j* of 45 mA cm^{-2}. The influence of illumination on H_2 production strongly depended on the applied *j*. At high *j*, H_2 generation is mainly dictated by the imposed electronic flux. This behavior is consistent with previous reports, where the contribution of photo-generated carriers becomes more relevant at lower current densities, reducing the required energy input, as reported in recent studies on biomass-assisted H_2 production [102]. This results in similar r_{H_2} values under dark and illuminated conditions, with light providing only a modest kinetic benefit. In contrast, at low *j*, illumination plays a dominant role by enhancing charge separation and reducing energy losses, which significantly lowers E_{con} and increases CEE, despite a lower absolute r_{H_2}. Overall cell voltage is largely

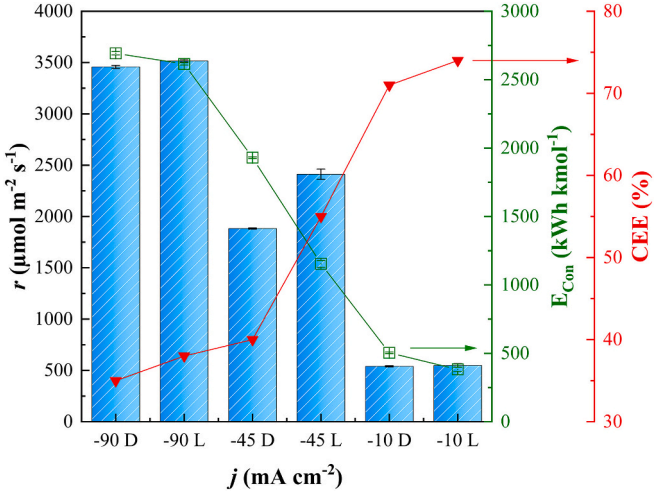

Fig. 8. H_2 production rate (r_{H_2}), E_{Con} (energy consumption), and CEE (cathodic energy efficiency) using the CWB photoanode in 0.5 M $KHCO_3$ + 1 M glycerol (anolyte) and 0.5 M $KHCO_3$ (catholyte) at different current densities under 1 sun back-illumination (100 mW cm^{-2}) – L and dark conditions – D. Legend: r_{H_2} (mmol m^{-2} s^{-1}), E_{Con} (kWh $kmol^{-1}$), CEE (%).

Table 5
Comparison of photoanode performance for assisted H_2 generation *via* PEC water splitting (100 mW cm^{-2}).

Photoanode composition	Electrolyte	r_{H_2} (μmol m^{-2} s^{-1})	*E*	*j* (mA cm^{-2})	Application	Ref.
$CaTiO_3/WO_3/BiVO_4$	0.5 M $KHCO_3$ (Catholyte)	549	−0.45 V *vs.* Ag/AgCl	10.0	GPEOR coupled with H_2 production	This work
$WO_3/BiVO_4/Bi$	0.5 M Na_2SO_4 + 0.1 M Glycerol	97	1.2 V *vs.* RHE	4.1	GPEOR coupled with H_2 production	[66]
Bi_2S_3/WO_3	0.1 M Na_2S + 0.1 M Na_2SO_3	161	−0.1 V *vs.* Ag/AgCl	7.0	PEC water splitting	[103]
$Zn_xBi_2S_{3+x}/WO_3$	0.1 M Na_2S + 0.1 M Na_2SO_3	267	−0.1 V *vs.* Ag/AgCl	7.0	PEC water splitting	[103]
$BiVO_4/TiO_2$	0.5 M $NaHCO_3$	85	2.08 V *vs.* RHE	5.5	PEC water splitting	[105]
$WO_3/BiVO_4$	1 M NaCl	131	1.75 V *vs.* RHE	3.4	PEC pollutant degradation coupled with H_2 production	[106]
$WO_3/BiVO_4$	1 M NaCl	106	1.75 V *vs.* RHE	2.7	PEC pollutant degradation coupled with H_2 production	[107]
$WO_3/BiVO_4/TiO_2$	0.1 M Na_2SO_4	89	1.23 V *vs.* RHE	4.2	PEC water splitting	[108]
$WO_3/BiVO_4/TiO_2$@200 °C (spray)/ 5 nm TiO_2 (sputtering)/NiOOH	0.5 M Na_2SO_4	206	2 V *vs.* RHE	5.3	PEC water splitting with concurrent recovery of Zinc (Zn^{2+}) from metal mine wastewater	[109]

influenced by the anodic contribution, particularly due to the multilayer photoanode architecture and the use of FTO substrates, which can increase internal resistance. In the absence of light, a higher potential is required to sustain the same current, reducing efficiency.

Although higher *j* yielded greater r_{H_2}, the system operated more efficiently at a lower *j* of −10 mA cm^{-2}, achieving an E_{con} of just 383 ± 15 kWh $kmol^{-1}$ and a CEE of 74% under illumination. At −10 mA cm^{-2} under irradiation, the r_{H_2} was 549 ± 18 μmol m^{-2} s^{-1}. Such performance highlights the system's ability to convert photogenerated electrons into H_2 with minimal energy loss. The H_2 Faradaic efficiency was found to be near-quantitative (approximately 100% within experimental uncertainty).

The CWB photoanode exhibited a r_{H_2} up to 6-fold higher than those of photoanodes presented in the literature made with similar materials, as seen in Table 5. For instance, the $Zn_xBi_2S_{3+x}/WO_3$ photoanode, the second-best performer, achieved a r_{H_2} of 265 μmol m^{-2} s^{-1}, which is less than half the r_{H_2} of the developed system [103]. Overall, the results obtained in this work align well with recent advances in the field compared to conventional EC water splitting systems. The use of glycerol not only reduces the thermodynamic and kinetic barriers to OER but also enables the co-production of value-added chemicals, reinforcing the relevance of this approach for sustainable energy applications [104].

4. Conclusions

In this study, a novel multilayered $CaTiO_3/WO_3/BiVO_4$ (CWB) heterostructured photoanode demonstrated significantly enhanced activity for GPEOR and H_2 production. The combined structural, morphological, and surface/cross-sectional analyses confirmed that the CWB photoanode was well-assembled, chemically stable, and compositionally coherent. The preserved oxidation states, controlled oxygen vacancies, and surface hydroxylation created favorable conditions for charge separation and molecular activation. At a fixed photocurrent density of −10 mA cm^{-2}, the photoanode promoted glycerol conversion into DHA, GEA, and $HCOO^-$ with an overall FE of 64%, achieving a DHA production rate of 124 ± 6 μmol m^{-2} s^{-1}. Concurrently, H_2 was produced at the cathode with a production rate of 549 ± 18 μmol m^{-2} s^{-1}, corresponding to an E_{Con} of 383 kWh $kmol^{-1}$ and a CEE of 74%. These findings highlight that GPEOR can significantly reduce energy requirements compared to OER while improving selectivity for desired products, underscoring the system's energy-saving potential. The multilayered CWB photoanode played a crucial role in achieving efficient light absorption, enhanced charge separation, and minimized recombination, leading to improved product selectivity and overall performance.

CRediT authorship contribution statement

Leonardo A. Delgado: Writing – review & editing, Writing – original draft, Visualization, Investigation, Formal analysis, Data curation. **Ivan Merino-Garcia:** Writing – review & editing, Validation, Supervision, Methodology, Investigation, Funding acquisition, Formal analysis, Data curation. **Sara Crespo:** Investigation, Formal analysis, Data curation. **Kevin Fernández-Caso:** Writing – review & editing, Validation, Methodology, Formal analysis, Data curation. **Vítor J.P. Vilar:** Supervision, Resources, Project administration, Funding acquisition, Conceptualization. **Francisca C. Moreira:** Writing – review & editing, Validation, Supervision, Resources, Project administration, Methodology, Investigation, Funding acquisition, Conceptualization. **Jonathan Albo:** Writing – review & editing, Validation, Supervision, Resources, Project administration, Methodology, Investigation, Funding acquisition, Formal analysis, Data curation, Conceptualization.

Declaration of competing interest

The authors declare the following financial interests/personal relationships which may be considered as potential competing interests: Given their role as Editor, Jonathan Albo had no involvement in the peer review of this article and had no access to information regarding its peer review. Full responsibility for the editorial process for this article was delegated to another journal editor. Given their role as Coordinating Editor, Vítor Vilar had no involvement in the peer review of this article and had no access to information regarding its peer review. Full responsibility for the editorial process for this article was delegated to another journal editor. If there are other authors, they declare that they have no known competing financial interests or personal relationships that could have appeared to influence the work reported in this paper.

Acknowledgments

This work was financially supported by Fundação para a Ciência e a Tecnologia, I.P./MCTES through national funds – LSRE-LCM, UID/50020/2025 (DOI: 10.54499/UID/50020/2025), and ALiCE, LA/P/0045/2020 (DOI: 10.54499/LA/P/0045/2020); and Spanish Grant PID2022-138491OB-C31 funded by MICIU/AEI/10.13039/501100011033 and by "ERDF/EU". Grant TED2021-129810B-C21 funded by MICIU/AEI/10.13039/501100011033 and by the "European Union NextGenerationEU/PRTR" is also acknowledged. Leonardo A. Delgado and Francisca C. Moreira acknowledge FCT for the financial support (references: 2021.07258.BD (DOI: 10.54499/2021.07258.BD), and 2023.07337.CEECIND/CP2834/CT0009 (DOI: 10.54499/2023.0

7337.CEECIND/CP2834/CT0009), respectively). Kevin Fernández-Caso acknowledges the financial support from the Spanish Grant PID2019-108136RB-C31. I. Merino-Garcia acknowledges Grant RYC2023-043378-I funded by MICIU/AEI/10.13039/501100011033 and by ESF+.

Appendix A. Supplementary data

Supplementary data to this article can be found online at https://doi.org/10.1016/j.cej.2026.177727.

Data availability

Data will be made available on request.

References

[1] C. Mota, B.P. Pinto, A. Lima, Glycerol: A versatile renewable feedstock for the chemical industry, Springer, Cham, Switzerland, 2017, https://doi.org/10.1007/978-3-319-59375-3.
[2] R. Ciriminna, C.D. Pina, M. Rossi, M. Pagliaro, Understanding the glycerol market, Eur. J. Lipid Sci. Technol. 116 (10) (2014) 1432–1439, https://doi.org/10.1002/ejlt.201400229.
[3] OECD-FAO, OECD-FAO Agricultural Outlook 2021–2030, Organisation for Economic Co-operation and Development and the Food and Agriculture Organization of the United Nations, Paris, France, 2021, https://doi.org/10.1787/19428846-en.
[4] Z. Gholami, A.Z. Abdullah, K.-T. Lee, Dealing with the surplus of glycerol production from biodiesel industry through catalytic upgrading to polyglycerols and other value-added products, Renew. Sust. Energ. Rev. 39 (2014) 327–341, https://doi.org/10.1016/j.rser.2014.07.092.
[5] P.J.M. Lima, R.M. da Silva, C.A.C.G. Neto, N.C. Gomes e Silva, J.E.d.S. Souza, Y. L. Nunes, J.C. Sousa dos Santos, An overview on the conversion of glycerol to value-added industrial products via chemical and biochemical routes, Biotechnol. Appl. Biochem. 69 (6) (2022) 2794–2818, https://doi.org/10.1002/bab.2098.
[6] W.L. Chow, S. Chong, J.W. Lim, Y.J. Chan, M.F. Chong, T.J. Tiong, J.K. Chin, G.-T. Pan, Anaerobic co-digestion of wastewater sludge: A review of potential co-substrates and operating factors for improved methane yield, Processes 8 (1) (2020) 39, https://doi.org/10.3390/pr8010039.
[7] A.J. Mattam, J.M. Clomburg, R. Gonzalez, S.S. Yazdani, Fermentation of glycerol and production of valuable chemical and biofuel molecules, Biotechnol. Lett. 35 (2013) 831–842, https://doi.org/10.1007/s10529-013-1240-4.
[8] M. Raza, A. Inayat, B. Abu-Jdayil, Crude glycerol as a potential feedstock for future energy via thermochemical conversion processes: A review, Sustainability 13 (22) (2021) 12813, https://doi.org/10.3390/su132212813.
[9] C.A. Schwengber, H.J. Alves, R.A. Schaffner, F.A. Da Silva, R. Sequinel, V. R. Bach, R.J. Ferracin, Overview of glycerol reforming for hydrogen production, Renew. Sust. Energ. Rev. 58 (2016) 259–266, https://doi.org/10.1016/j.rser.2015.12.279.
[10] Y.-C. Lin, Catalytic valorization of glycerol to hydrogen and syngas, Int. J. Hydrog. Energy 38 (6) (2013) 2678–2700, https://doi.org/10.1016/j.ijhydene.2012.12.079.
[11] S. Bagheri, N.M. Julkapli, W.A. Yehye, Catalytic conversion of biodiesel derived raw glycerol to value added products, Renew. Sust. Energ. Rev. 41 (2015) 113–127, https://doi.org/10.1016/j.rser.2014.08.031.
[12] C.H. Zhou, H. Zhao, D.S. Tong, L.M. Wu, W.H. Yu, Recent advances in catalytic conversion of glycerol, Catal. Rev. 55 (4) (2013) 369–453, https://doi.org/10.1080/01614940.2013.816610.
[13] Y. Miao, M. Shao, Photoelectrocatalysis for high-value-added chemicals production, Chin. J. Catal. 43 (3) (2022) 595–610, https://doi.org/10.1016/S1872-2067(21)63923-2.
[14] F. Vitulano, F. Uggeri, L. Lattuada, A. Minguzzi, A. Vertova, Tackling electrocatalytic oxidation of glycerol to dihydroxyacetone: A comprehensive review, Curr. Opin. Electrochem. (2025) 101665, https://doi.org/10.1016/j.coelec.2025.101665.
[15] X. Guo, R.-T. Gao, S. Ren, N.T. Nguyen, H. Chen, L. Wu, L. Wang, Direct ammonia and dihydroxyacetone production in an unbiased photoelectrochemical cell, Nat. Commun. 16 (1) (2025) 6220, https://doi.org/10.1038/s41467-025-61080-x.
[16] J.-A. Lin, I. Roh, P. Yang, Photochemical diodes for simultaneous bias-free glycerol valorization and hydrogen evolution, J. Am. Chem. Soc. 145 (24) (2023) 12987–12991, https://doi.org/10.1021/jacs.3c01982.
[17] M.D. Makhafola, S.A. Balogun, K.D. Modibane, A comprehensive review of bimetallic nanoparticle–graphene oxide and bimetallic nanoparticle–metal–organic framework nanocomposites as photo-, electro-, and photoelectrocatalysts for hydrogen evolution reaction, Energies 17 (7) (2024) 1646, https://doi.org/10.3390/en17071646.
[18] E. Antolini, Glycerol electro-oxidation in alkaline media and alkaline direct glycerol fuel cells, Catalysts 9 (12) (2019) 980, https://doi.org/10.3390/catal9120980.
[19] A.J. Bard, L.R. Faulkner, Electrochemical methods: fundamentals and applications, Second ed., John Wiley & Sons, New York, USA, 2001.
[20] Z. Ke, N. Williams, X. Yan, S. Younan, D. He, X. Song, X. Pan, X. Xiao, J. Gu, Solar-assisted co-electrolysis of glycerol and water for concurrent production of formic acid and hydrogen, J. Mater. Chem. A 9 (35) (2021) 19975–19983, https://doi.org/10.1039/D1TA02654B.
[21] G. Wu, X. Dong, J. Mao, G. Li, C. Zhu, S. Li, A. Chen, G. Feng, Y. Song, W. Chen, Anodic glycerol oxidation to formate facilitating cathodic hydrogen evolution with earth-abundant metal oxide catalysts, Chem. Eng. J. 468 (2023) 143640, https://doi.org/10.1016/j.cej.2023.143640.
[22] Y. Yan, P. Hao, Y. Fu, W. Chen, Q. Shi, H. Zhou, X. Kong, Z. Li, M. Shao, X. Duan, Selective electrooxidation glycerol to lactic acid coupled with hydrogen production over a cooperative BiOx/Au catalyst, AICHE J. 70 (5) (2024) e18370, https://doi.org/10.1002/aic.18370.
[23] A. Ali, M. Qasim, S. Sakhi, G. Maduraiveeran, A.S. Alnaser, Electrochemical CO2 reduction: advances, insights, challenges, and future directions, Mater. Today Sustain. (2025) 101089, https://doi.org/10.1016/j.mtsust.2025.101089.
[24] Á. Balog, E. Kecsenovity, G.F. Samu, J. He, D. Fekete, C. Janáky, Paired photoelectrochemical conversion of CO_2/H_2O and glycerol at high rate, Nat. Catal. (2024) 1–14, https://doi.org/10.1038/s41929-024-01134-3.
[25] S. Zhou, Y. Dai, Q. Song, L. Lu, X. Yu, Efficient bi-functional catalyst towards coupling glycerol oxidation and CO_2 reduction to achieve formic acid and formate production, J. Electroanal. Chem. 957 (2024) 118133, https://doi.org/10.1016/j.jelechem.2024.118133.
[26] J.A. Abarca, G. Díaz-Sainz, I. Merino-Garcia, A. Irabien, J. Albo, Photoelectrochemical CO2 electrolyzers: from photoelectrode fabrication to reactor configuration, J. Energy Chem. (2023), https://doi.org/10.1016/j.jechem.2023.06.032.
[27] H. Abdullah, H. Shuwanto, J. Lie, M. Sillanpää, Critical parameters and essential strategies in designing photoanodes to overcome the sluggish water oxidation reaction, J. Environ. Chem. Eng. 11 (2) (2023) 109356, https://doi.org/10.1016/j.jece.2023.109356.
[28] R. Chong, B. Wang, D. Li, Z. Chang, L. Zhang, Enhanced photoelectrochemical activity of Nickel-phosphate decorated phosphate-Fe_2O_3 photoanode for glycerol-based fuel cell, Sol. Energy Mater. Sol. Cells 160 (2017) 287–293, https://doi.org/10.1016/j.solmat.2016.10.052.
[29] L. Luo, W. Chen, S.-M. Xu, J. Yang, M. Li, H. Zhou, M. Xu, M. Shao, X. Kong, Z. Li, Selective photoelectrocatalytic glycerol oxidation to dihydroxyacetone via enhanced middle hydroxyl adsorption over a Bi_2O_3-incorporated catalyst, J. Am. Chem. Soc. 144 (17) (2022) 7720–7730, https://doi.org/10.1021/jacs.2c00465.
[30] L.-W. Huang, T.-G. Vo, C.-Y. Chiang, Converting glycerol aqueous solution to hydrogen energy and dihydroxyacetone by the $BiVO_4$ photoelectrochemical cell, Electrochim. Acta 322 (2019) 134725, https://doi.org/10.1016/j.electacta.2019.134725.
[31] J. Yu, J. González-Cobos, F. Dappozze, N. Grimaldos-Osorio, P. Vernoux, A. Caravaca, C. Guillard, First PEM photoelectrolyser for the simultaneous selective glycerol valorization into value-added chemicals and hydrogen generation, Appl. Catal. B Environ. 327 (2023) 122465, https://doi.org/10.1016/j.apcatb.2023.122465.
[32] Y. Lee, S. Kim, S.Y. Jeong, S. Seo, C. Kim, H. Yoon, H.W. Jang, S. Lee, Surface-Modified Co-doped ZnO photoanode for photoelectrochemical oxidation of glycerol, Catal. Today 359 (2021) 43–49, https://doi.org/10.1016/j.cattod.2019.06.065.
[33] B. Brasiunas, A. Popov, V. Lisyte, A. Kausaite-Minkstimiene, A. Ramanaviciene, ZnO nanostructures: a promising frontier in immunosensor development, Biosens. Bioelectron. (2023) 115848, https://doi.org/10.1016/j.bios.2023.115848.
[34] P. Mane, V. Burungale, H. Bae, C. Seong, J. Heo, S.-W. Ryu, S.-H. Kang, J.-S. Ha, Empowering metal oxide photoanodes via zeolitic imidazolate frameworks for efficient photoelectrochemical water splitting: Current advances and future perspectives, Renew. Sust. Energ. Rev. 202 (2024) 114671, https://doi.org/10.1016/j.rser.2024.114671.
[35] S. Giménez, J. Bisquert, Photoelectrochemical solar fuel production: from basic principle to advanced devices, Springer, Cham, Switzerland, 2016, https://doi.org/10.1007/978-3-319-29641-8.
[36] L. Oliveira, A. De Moura, F. La Porta, I. Nogueira, E. Aguiar, T. Sequinel, I. Rosa, E. Longo, J. Varela, Influence of Cu-doping on the structural and optical properties of $CaTiO_3$ powders, Mater. Res. Bull. 81 (2016) 1–9, https://doi.org/10.1016/j.materresbull.2016.04.024.
[37] M.G. Lee, W. Sohn, C.W. Moon, H. Park, S. Lee, H.W. Jang, Conformally coated $BiVO_4$ nanodots on porosity-controlled WO_3 nanorods as highly efficient type II heterojunction photoanodes for water oxidation, Nano Energy 28 (2016) 250–260, https://doi.org/10.1016/j.nanoen.2016.08.046.
[38] D. Chen, Z. Xie, Y. Tong, Y. Huang, Review on $BiVO_4$-based photoanodes for photoelectrochemical water oxidation: the main influencing factors, Energy Fuel 36 (17) (2022) 9932–9949, https://doi.org/10.1021/acs.energyfuels.2c02119.
[39] Z.F. Huang, J. Song, L. Pan, X. Zhang, L. Wang, J.J. Zou, Tungsten oxides for photocatalysis, electrochemistry, and phototherapy, Adv. Mater. 27 (36) (2015) 5309–5327, https://doi.org/10.1002/adma.201501217.
[40] J.A. Abarca, I. Merino-Garcia, G. Díaz-Sainz, M. Perfecto-Irigaray, G. Beobide, A. Irabien, J. Albo, Fabrication and optimization of perovskite-based photoanodes for solar-driven CO_2 photoelectroreduction to formate, Catal. Today 429 (2024) 114505, https://doi.org/10.1016/j.cattod.2023.114505.
[41] I. Merino-Garcia, S. Crespo, M. Perfecto-Irigaray, G. Beobide, A. Irabien, J. Albo, Tailoring multi-layered $BiVO_4$/WO_3 photoanodes for an efficient photoelectrochemical gas-phase solar water splitting, Catal. Today 432 (2024) 114581, https://doi.org/10.1016/j.cattod.2024.114581.
[42] S.A.U. Portia, R. Srinivasan, E. Elaiyappillai, P.M. Johnson, K. Ramamoorthy, Facile synthesis of Eu-doped $CaTiO_3$ and their enhanced supercapacitive

performance, Ionics 26 (2020) 3543–3554, https://doi.org/10.1007/s11581-020-03494-9.
[43] S. Castro, J. Albo, A. Irabien, Continuous conversion of CO_2 to alcohols in a TiO_2 photoanode-driven photoelectrochemical system, J. Chem. Technol. Biotechnol. 95 (7) (2020) 1876–1882, https://doi.org/10.1002/jctb.6315.
[44] I. Merino-Garcia, J. Albo, A. Irabien, Tailoring gas-phase CO_2 electroreduction selectivity to hydrocarbons at Cu nanoparticles, Nanotechnology 29 (1) (2017) 014001, https://doi.org/10.1088/1361-6528/aa994e.
[45] G. Díaz-Sainz, J.A. Abarca, M. Alvarez-Guerra, A. Irabien, Exploring the impact of partial pressure and typical compounds on the continuous electroconversion of CO_2 into formate, J. CO_2 Util. 81 (2024) 102735, https://doi.org/10.1016/j.jcou.2024.102735.
[46] I. Merino-Garcia, L. Tinat, J. Albo, M. Alvarez-Guerra, A. Irabien, O. Durupthy, V. Vivier, C.M. Sánchez-Sánchez, Continuous electroconversion of CO_2 into formate using 2 nm tin oxide nanoparticles, Appl. Catal. B Environ. 297 (2021) 120447, https://doi.org/10.1016/j.apcatb.2021.120447.
[47] K. Fernández-Caso, A. Pena-Rodríguez, J. Solla-Gullón, V. Montiel, G. Díaz-Sainz, M. Alvarez-Guerra, A. Irabien, Continuous carbon dioxide electroreduction to formate coupled with the single-pass glycerol oxidation to high value-added products, J. CO_2 Util. 70 (2023) 102431, https://doi.org/10.1016/j.jcou.2023.102431.
[48] S.K. Saraswat, D.D. Rodene, R.B. Gupta, Recent advancements in semiconductor materials for photoelectrochemical water splitting for hydrogen production using visible light, Renew. Sust. Energ. Rev. 89 (2018) 228–248, https://doi.org/10.1016/j.rser.2018.03.063.
[49] J. Yu, J. Gonzalez-Cobos, F. Dappozze, F.J. Lopez-Tenllado, J. Hidalgo-Carrillo, A. Marinas, P. Vernoux, A. Caravaca, C. Guillard, WO_3-based materials for photoelectrocatalytic glycerol upgrading into glyceraldehyde: Unravelling the synergistic photo-and electro-catalytic effects, Appl. Catal. B Environ. 318 (2022) 121843, https://doi.org/10.1016/j.apcatb.2022.121843.
[50] K. Fernández-Caso, M. Molera, T. Andreu, J. Solla-Gullón, V. Montiel, G. Díaz-Sainz, M. Álvarez-Guerra, A. Irabien, Coupling glycerol oxidation reaction using Ni-Co foam anodes to CO_2 electroreduction in gas-phase for continuous co-valorization, Chem. Eng. J. 480 (2024) 147908, https://doi.org/10.1016/j.cej.2023.147908.
[51] F. Amano, Photoelectrochemical Oxygen Evolution, Solar-to-chemical conversion: Photocatalytic and photoelectrochemcial processes (2021) 163–187, https://doi.org/10.1002/9783527825073.ch7.
[52] T.J. Smith, K.J. Stevenson, Handbook of electrochemistry, Elsevier Science, New Mexico, USA, 2007, https://doi.org/10.1016/B978-0-444-51958-0.X5000-9.
[53] Z. Chen, H.N. Dinh, E. Miller, Photoelectrochemical water splitting: Standards, experimental methods, and protocols, Springer, New York, USA, 2013, https://doi.org/10.1007/978-1-4614-8298-7.
[54] I. Merino-Garcia, J. Albo, J. Solla-Gullón, V. Montiel, A. Irabien, Cu oxide/ZnO-based surfaces for a selective ethylene production from gas-phase CO_2 electroconversion, J. CO_2 Util. 31 (2019) 135–142, https://doi.org/10.1016/j.jcou.2019.03.002.
[55] S. Zhang, M. Rohloff, O. Kasian, A.M. Mingers, K.J. Mayrhofer, A. Fischer, C. Scheu, S. Cherevko, Dissolution of $BiVO_4$ photoanodes revealed by time-resolved measurements under photoelectrochemical conditions, J. Phys. Chem. C 123 (38) (2019) 23410–23418, https://doi.org/10.1021/acs.jpcc.9b07220.
[56] H. Wen, Z. Pan, X. Wang, K. Li, Q. Wang, J. Luo, H. Fu, L. Zhang, Z. Wang, Dissolution behaviors of a visible-light-responsive photocatalyst $BiVO_4$: Measurements and chemical equilibrium modeling, J. Hazard. Mater. 443 (2023) 130187, https://doi.org/10.1016/j.jhazmat.2022.130187.
[57] J. Kim, H.J. Choi, H. Choi, S.Y. Kang, H. Choi, C.Y. Ahn, Y. Kim, I. La, O.H. Kim, Y.H. Cho, Optimization of ionomer for high-performance self-humidifying air-breathing proton-exchange membrane fuel cells in portable device power systems, Energy Technol. 13 (1) (2025) 2400445, https://doi.org/10.1002/ente.202400445.
[58] C. Han, J. Liu, W. Yang, Q. Wu, H. Yang, X. Xue, Photocatalytic activity of $CaTiO_3$ synthesized by solid state, sol–gel and hydrothermal methods, J. Sol-Gel Sci. Technol. 81 (2017) 806–813, https://doi.org/10.1007/s10971-016-4261-3.
[59] W.L. Kwong, P. Koshy, J.N. Hart, W. Xu, C.C. Sorrell, Critical role of {002} preferred orientation on electronic band structure of electrodeposited monoclinic WO_3 thin films, Sustain. Energy Fuels 2 (10) (2018) 2224–2236, https://doi.org/10.1039/C8SE00239H.
[60] M. Jamali, F.S. Tehrani, Thermally stable WO_3 nanostructure synthesized by hydrothermal method without using surfactant, Mater. Sci. Eng. B 270 (2021) 115221, https://doi.org/10.1016/j.mseb.2021.115221.
[61] P. Pookmanee, K. Pingmuang, W. Kangwansupamonkon, S. Phanichphant, Methylene blue degradation over photocatalyst bismuth vanadate powder synthesized by the hydrothermal method, Adv. Mater. Res. 93 (2010) 177–180, https://doi.org/10.4028/www.scientific.net/AMR.93-94.177.
[62] K. Zhong, H. Gao, J. Feng, Y. Zhang, K. Lai, Facile synthesis of Z-scheme Se/$BiVO_4$ heterojunction with enhanced visible-light-driven photocatalytic performance, J. Mater. Sci. 54 (15) (2019) 10632–10643, https://doi.org/10.1007/s10853-019-03634-1.
[63] M.A. Ehsan, R. Naeem, V. McKee, A. Rehman, A.S. Hakeem, M. Mazhar, Fabrication of photoactive $CaTiO_3$–TiO_2 composite thin film electrodes via facile single step aerosol assisted chemical vapor deposition route, J. Mater. Sci. Mater. Electron. 30 (2019) 1411–1424, https://doi.org/10.1007/s10854-018-0411-4.
[64] H. Zhang, Y. He, M. He, Q. Yang, G. Ding, Y. Mo, Z. Liu, P. Gao, Construction of cubic $CaTiO_3$ perovskite modified by highly-dispersed cobalt for efficient catalytic degradation of psychoactive pharmaceuticals, J. Hazard. Mater. 459 (2023) 132191, https://doi.org/10.1016/j.jhazmat.2023.132191.
[65] L. Sharma, P. Kumar, A. Halder, Phase and vacancy modulation in tungsten oxide: electrochemical hydrogen evolution, ChemElectroChem 6 (13) (2019) 3420–3428, https://doi.org/10.1002/celc.201900666.
[66] X. Feng, X. Feng, F. Zhang, Enhanced photoelectrochemical oxidation of glycerol to dihydroxyacetone coupled with hydrogen generation via accelerative middle hydroxyl dehydrogenation over a Bi^0/Bi^{3+} interface of a cascade heterostructure, J. Mater. Chem. A 11 (37) (2023) 20242–20253, https://doi.org/10.1039/D3TA04326F.
[67] K.R. Tolod, T. Saboo, S. Hernández, H. Guzmán, M. Castellino, R. Irani, P. Bogdanoff, F.F. Abdi, E.A. Quadrelli, N. Russo, Insights on the surface chemistry of $BiVO_4$ photoelectrodes and the role of Al overlayers on its water oxidation activity, Appl. Catal. A Gen. 605 (2020) 117796, https://doi.org/10.1016/j.apcata.2020.117796.
[68] Y. Lu, B.G. Lee, C. Lin, T.-K. Liu, Z. Wang, J. Miao, S.H. Oh, K.C. Kim, K. Zhang, J. H. Park, Solar-driven highly selective conversion of glycerol to dihydroxyacetone using surface atom engineered $BiVO_4$ photoanodes, Nat. Commun. 15 (1) (2024) 5475, https://doi.org/10.1038/s41467-024-49662-7.
[69] K. Onwuka, C. Aghalibe, U. Nkwoada, J. Igwe, C. Osigwe, K. Eze, Comprehensive review on the efficacy of alkylammonium cation pillared clays for sorption of volatile organic carbons, J. Chem. Res. 4 (6) (2019) 87–108.
[70] N. Rezlescu, E. Rezlescu, P.D. Popa, C. Doroftei, M. Ignat, Characterization and catalytic properties of some perovskites, Compos. Part B Eng. 60 (2014) 515–522, https://doi.org/10.1016/j.compositesb.2014.01.006.
[71] T. Hamada, A.R. Circelli, H. Inoue, C.A. Randall, E.L. Clark, Investigating the Origins of the pH-Dependent Oxidation of Glycerol over Platinum Using Differential Electrochemical Mass Spectrometry, J. Phys. Chem. C 128 (26) (2024) 10790–10801, https://doi.org/10.1021/acs.jpcc.4c01372.
[72] C.G. Ferreira, C. Ros, M. Zhang, G. Zhou, V. Gacha, D. Raptis, I.D. Sharp, J. Martorell, Sub-bandgap photon-to-current conversion in bismuth vanadate photoanodes and its impact on the maximum photocurrent density achievable for water splitting, ACS Energy Lett. 10 (9) (2025) 4332–4341, https://doi.org/10.1021/acsenergylett.5c01894.
[73] Q. Yi, H. Wang, J.M. Lee, $BiVO_4$-based photoelectrochemical water splitting, ChemElectroChem 12 (4) (2025) e202400600, https://doi.org/10.1002/celc.202400600Digital Object Identifier (DOI).
[74] M.C. Haryanto, R. Hartanto, T.-G. Vo, C.-Y. Chiang, Factors affecting selective electrochemical glycerol oxidation to three-carbon products over cuprous oxide microcubes, J. Taiwan Inst. Chem. Eng. 158 (2024) 105087, https://doi.org/10.1016/j.jtice.2023.105087.
[75] S. Xu, D. Fu, K. Song, L. Wang, Z. Yang, W. Yang, H. Hou, One-dimensional WO_3/$BiVO_4$ heterojunction photoanodes for efficient photoelectrochemical water splitting, Chem. Eng. J. 349 (2018) 368–375, https://doi.org/10.1016/j.cej.2018.05.100.
[76] P. Długołęcki, P. Ogonowski, S.J. Metz, M. Saakes, K. Nijmeijer, M. Wessling, On the resistances of membrane, diffusion boundary layer and double layer in ion exchange membrane transport, J. Membr. Sci. 349 (1–2) (2010) 369–379, https://doi.org/10.1016/j.memsci.2009.11.069.
[77] I. Grigioni, M. Abdellah, A. Corti, M.V. Dozzi, L. Hammarström, E. Selli, Photoinduced charge-transfer dynamics in WO_3/$BiVO_4$ photoanodes probed through midinfrared transient absorption spectroscopy, J. Am. Chem. Soc. 140 (43) (2018) 14042–14045, https://doi.org/10.1021/jacs.8b08309.
[78] S. Crespo, I. Merino-Garcia, M. Perfecto-Irigaray, G. Beobide, J. Albo, Stable Ni-decorated $CaTiO_3$/WO_3/$BiVO_4$ multi-layered photoanodes for improved solar-driven water oxidation at high current densities, J. Environ. Chem. Eng. (2025) 118854, https://doi.org/10.1016/j.jece.2025.118854.
[79] I. Grigioni, A. Polo, M.V. Dozzi, K.G. Stamplecoskie, D.H. Jara, P.V. Kamat, E. Selli, Enhanced charge carrier separation in WO_3/$BiVO_4$ photoanodes achieved via light absorption in the $BiVO_4$ layer, ACS Appl. Energy Mater. 5 (11) (2022) 13142–13148, https://doi.org/10.1021/acsaem.2c02597.
[80] S.N.S. Nasir, N.A. Mohamed, M.A. Tukimon, M.F.M. Noh, N.A. Arzaee, M.A. M. Teridi, Direct extrapolation techniques on the energy band diagram of $BiVO_4$ thin films, Phys. B Condens. Matter 604 (2021) 412719, https://doi.org/10.1016/j.physb.2020.412719.
[81] R. Radha, A. Srinivasan, P. Manimuthu, S. Balakumar, Tailored sunlight driven nano-photocatalyst: bismuth iron tungstate ($BiFeWO_6$), J. Mater. Chem. C 3 (39) (2015) 10285–10292, https://doi.org/10.1039/C4TC02284J.
[82] Y. Zhang, L. Xu, B. Liu, X. Wang, T. Wang, X. Xiao, S. Wang, W. Huang, Engineering $BiVO_4$ and oxygen evolution cocatalyst interfaces with rapid hole extraction for photoelectrochemical water splitting, ACS Catal. 13 (9) (2023) 5938–5948, https://doi.org/10.1021/acscatal.3c00444.
[83] A. Polo, C. Nomellini, G. Marra, E. Selli, M.V. Dozzi, WO_3/$BiVO_4$ heterojunction photoanodes: Optimized photoelectrochemical performance in relation to both oxides layer thickness, Catal. Today 446 (2025) 115137, https://doi.org/10.1016/j.cattod.2024.115137.
[84] X. Shi, I. Herraiz-Cardona, L. Bertoluzzi, P. Lopez-Varo, J. Bisquert, J.H. Park, S. Gimenez, Understanding the synergistic effect of WO_3–$BiVO_4$ heterostructures by impedance spectroscopy, Phys. Chem. Chem. Phys. 18 (13) (2016) 9255–9261, https://doi.org/10.1039/C5CP07905E.
[85] X. Zhong, Y. Li, H. Wu, R. Xie, Recent progress in $BiVO_4$-based heterojunction nanomaterials for photocatalytic applications, Mater. Sci. Eng. B 289 (2023) 116278, https://doi.org/10.1016/j.mseb.2023.116278.
[86] S.J. Hong, S. Lee, J.S. Jang, J.S. Lee, Heterojunction $BiVO_4$/WO_3 electrodes for enhanced photoactivity of water oxidation, Energy Environ. Sci. 4 (5) (2011) 1781–1787, https://doi.org/10.1039/C0EE00743A.
[87] J. Zhang, Y. Yan, A. Armutlulu, K. Wei, J. Wu, B. Lai, R. Xie, Assembling a durable homologous-like heterojunction s-TiO_2@$CaTiO_3$ for photodegradation of atrazine

through boosting charge migration with peroxymonosulfate reinforcement, Chem. Eng. J. 490 (2024) 151300, https://doi.org/10.1016/j.cej.2024.151300.
[88] H. Lv, C. Zhou, Q. Shen, Y. Kong, B. Wan, Z. Suo, G. Wang, G. Wang, Y. Liu, Rationally designed $CaTiO_3/Mn_{0.5}Cd_{0.5}S/Ni_3C$ S-scheme/Schottky integrated heterojunction for efficient photocatalytic H_2 evolution, J. Colloid Interface Sci. 677 (2025) 365–376, https://doi.org/10.1016/j.jcis.2024.08.072.
[89] M. Passi, B. Pal, A review on $CaTiO_3$ photocatalyst: Activity enhancement methods and photocatalytic applications, Powder Technol. 388 (2021) 274–304, https://doi.org/10.1016/j.powtec.2021.04.056.
[90] I. Grigioni, G. Di Liberto, M.V. Dozzi, S. Tosoni, G. Pacchioni, E. Selli, $WO_3/BiVO_4$ photoanodes: facets matching at the heterojunction and $BiVO_4$ layer thickness effects, ACS Appl. Energy Mater. 4 (8) (2021) 8421–8431, https://doi.org/10.1021/acsaem.1c01623.
[91] A. Kormányos, A. Szirmai, B. Endrodi, C. Janáky, Stable operation of paired CO_2 reduction/glycerol oxidation at high current density, ACS Catal. 14 (9) (2024) 6503–6512, https://doi.org/10.1021/acscatal.3c05952.
[92] A. Peña-Rodríguez, K. Fernández-Caso, G. Díaz-Sainz, M. Álvarez-Guerra, V. Montiel, J. Solla-Gullon, Single-pass electrooxidation of glycerol on bismuth-modified platinum electrodes as an anodic process coupled to the continuous CO_2 electroreduction toward formate, ACS Sustain. Chem. Eng. 12 (9) (2024) 3671–3679, https://doi.org/10.1021/acssuschemeng.3c07131.
[93] H. Chen, R.T. Gao, K. Su, Z. Li, L. Wu, L. Wang, Re and Ru Co-Doped Transition Metal Alloy as a Bifunctional Catalyst for Electrooxidation of Glycerol to Formate Coupled with H_2 Production, Angew. Chem. 137 (20) (2025) e202501766, https://doi.org/10.1002/anie.202501766.
[94] H. Chen, R.T. Gao, F. Yang, L. Wu, L. Wang, High-Selectivity Electrocatalytic Oxidation of Glycerol to C_3-Glyceraldehyde Coupled to H_2O_2 Production, Angew. Chem. 137 (48) (2025) e202514737, https://doi.org/10.1002/ange.202514737.
[95] Y.-H. Wu, D.A. Kuznetsov, N.C. Pflug, A. Fedorov, C.R. Müller, Solar-driven valorisation of glycerol on $BiVO_4$ photoanodes: effect of co-catalyst and reaction media on reaction selectivity, J. Mater. Chem. A 9 (10) (2021) 6252–6260, https://doi.org/10.1039/D0TA10480A.
[96] Z. Gu, X. An, R. Liu, L. Xiong, J. Tang, C. Hu, H. Liu, J. Qu, Interface-modulated nanojunction and microfluidic platform for photoelectrocatalytic chemicals upgrading, Appl. Catal. B Environ. 282 (2021) 119541, https://doi.org/10.1016/j.apcatb.2020.119541.
[97] T.-G. Vo, C.-C. Kao, J.-L. Kuo, C.-c. Chiu, C.-Y. Chiang, Unveiling the crystallographic facet dependence of the photoelectrochemical glycerol oxidation on bismuth vanadate, Appl. Catal. B Environ. 278 (2020) 119303, https://doi.org/10.1016/j.apcatb.2020.119303.
[98] H. Kong, S. Gupta, A.F. Pérez-Torres, C. Höhn, P. Bogdanoff, M.T. Mayer, R. van de Krol, M. Favaro, F.F. Abdi, Electrolyte selection toward efficient photoelectrochemical glycerol oxidation on $BiVO_4$, Chem. Sci. 15 (27) (2024) 10425–10435, https://doi.org/10.1039/d4sc01651c.
[99] J. Ouyang, X. Liu, B.-H. Wang, J.-B. Pan, S. Shen, L. Chen, C.-T. Au, S.-F. Yin, WO_3 photoanode with predominant exposure of {202} facets for enhanced selective oxidation of glycerol to glyceraldehyde, ACS Appl. Mater. Interfaces 14 (20) (2022) 23536–23545, https://doi.org/10.1021/acsami.2c04608.
[100] H. Tateno, S.-Y. Chen, Y. Miseki, T. Nakajima, T. Mochizuki, K. Sayama, Photoelectrochemical oxidation of glycerol to dihydroxyacetone over an acid-resistant Ta: $BiVO_4$ photoanode, ACS Sustain. Chem. Eng. 10 (23) (2022) 7586–7594, https://doi.org/10.1021/acssuschemeng.2c01282.
[101] Z. Yang, H. Chen, S. Bei, K. Bao, C. Zhang, M. Xiang, C. Yu, S. Dong, H. Qin, Ultralow RuO_2 doped NiS_2 heterojunction as a multifunctional electrocatalyst for hydrogen evolution linking to biomass organics oxidation, Small 20 (24) (2024) 2310286, https://doi.org/10.1002/smll.202310286Digital.
[102] Z. Yang, K. Qian, Z. Zhang, S. Dong, J. Hui, C. Yu, W. Fan, Rare-earth metal based $Pr/Pr_2(SeO_3)_3$ Mott-Schottky heterojunction for electrocatalytic water splitting to produce hydrogen linking to organics oxidation, Int. J. Hydrog. Energy 68 (2024) 202–208, https://doi.org/10.1016/j.ijhydene.2024.04.156.
[103] C. Liu, Y. Yang, W. Li, J. Li, Y. Li, Q. Shi, Q. Chen, Highly efficient photoelectrochemical hydrogen generation using $Zn_x Bi_2S_{3+x}$ sensitized platelike WO_3 photoelectrodes, ACS Appl. Mater. Interfaces 7 (20) (2015) 10763–10770, https://doi.org/10.1021/acsami.5b00830.
[104] X. Xie, C. Zhang, M. Xiang, C. Yu, W. Fan, S. Dong, Z. Yang, $SnO_2/CoS_{1.097}$ heterojunction as a green electrocatalyst for hydrogen evolution linking to assistant glycerol oxidation, Green Chem. 25 (22) (2023) 9405–9412, https://doi.org/10.1039/D3GC03534D.
[105] O. Monfort, D. Raptis, L. Satrapinskyy, T. Roch, G. Plesch, P. Lianos, Production of hydrogen by water splitting in a photoelectrochemical cell using a $BiVO_4/TiO_2$ layered photoanode, Electrochim. Acta 251 (2017) 244–249, https://doi.org/10.1016/j.electacta.2017.08.125.
[106] K.R. Davies, M.G. Allan, S. Nagarajan, R. Townsend, T. Dunlop, J.D. McGettrick, V.S. Asokan, S. Ananthraj, T. Watson, A.R. Godfrey, Solar light-driven simultaneous pharmaceutical pollutant degradation and green hydrogen production using a mesoporous nanoscale $WO_3/BiVO_4$ heterostructure photoanode, J. Environ. Chem. Eng. 11 (3) (2023) 110256, https://doi.org/10.1016/j.jece.2023.110256.
[107] K.R. Davies, M.G. Allan, S. Nagarajan, R. Townsend, V. Asokan, T. Watson, A. R. Godfrey, M.M. Maroto-Valer, M.F. Kuehnel, S. Pitchaimuthu, Photoelectrocatalytic Surfactant Pollutant Degradation and Simultaneous Green Hydrogen Generation, Ind. Eng. Chem. Res. 62 (45) (2023) 19084–19094, https://doi.org/10.1021/acs.iecr.3c00840.
[108] S.S. Kalanur, I.-H. Yoo, J. Park, H. Seo, Insights into the electronic bands of $WO_3/BiVO_4/TiO_2$, revealing high solar water splitting efficiency, J. Mater. Chem. A 5 (4) (2017) 1455–1461, https://doi.org/10.1039/C6TA07592D.
[109] L. Thirumalaisamy, Z. Wei, K.R. Davies, M.G. Allan, J. McGettrick, T. Watson, M. F. Kuehnel, S. Pitchaimuthu, Dual shield: Bifurcated coating analysis of multilayered $WO_3/BiVO_4/TiO_2/NiOOH$ photoanodes for sustainable solar-to-hydrogen generation from challenging waters, ACS Sustain. Chem. Eng. 12 (8) (2024) 3044–3060, https://doi.org/10.1021/acssuschemeng.3c06528.